Chapter 3

SOLAR WIND

J. Feynman

The solar wind or interplanetary medium is a fully ionized, electrically neutral plasma that carries a magnetic field and streams outward from the inner solar corona at all times. The wind is highly variable in both time and space and fills the interstellar region in the vicinity of the sun. This chapter describes the observed properties of the solar wind in the vicinity of the earth, including the undisturbed wind and the magnetosheath and bow shock formed as the solar wind flows around the earth's magnetic field.

3.1 BASIC THEORY

3.1.1 Simple Spherically Symmetric Treatment

The solar wind is the outer part of the sun's corona, streaming past the earth. Chapman [1957] made an early estimate of the particle density expected in space at the orbit of the earth. He considered the expansion of a corona with a temperature at the base on the order of 10^6 K. He calculated the coronal density profile assuming that the corona was in hydrostatic equilibrium and found that the electron density at the earth's orbit would be 10^2 or 10^3 particles/cm^3. He also found that the pressure at large heliocentric distances would be of the order of 10^{-5} dyn/cm^2, whereas estimates of the interstellar pressure were in the range of 10^{-12} or 10^{-13} dyn/cm^2. Thus, the hydrostatic corona could not be matched with its boundary conditions in the distant heliosphere. This treatment, although describing the sun in a very simplified manner, led Parker to postulate that the corona was not in hydrostatic equilibrium and that, in fact, the coronal plasma was flowing out from the sun continuously. Parker [1963] treated the problem as that of a steady state spherically symmetric fluid expansion. The equations that govern the behavior of such a system are the equations of mass, momentum, and energy conservation. The mass conservation is expressed by

$$\frac{1}{r^2} \frac{d}{dr} (r^2 \rho u) = 0, \qquad (3.1)$$

where r is the radial distance, ρ the mass density, and u the radial velocity. The momentum equation for a fluid is written as

$$\rho u \frac{du}{dr} = \frac{-dP}{dr} - \rho \frac{GM_o}{r^2}, \qquad (3.2)$$

where P is the scalar pressure, G the gravitational constant, and M_o the mass of the sun. Energy conservation is given by

$$\frac{1}{r^2} \frac{d}{dr} \left[r^2 \rho u \left(\frac{1}{2} u^2 + \frac{3}{2} \frac{P}{\rho} \right) \right] \qquad (3.3)$$

$$= \frac{-1}{r^2} \frac{d}{dr} (r^2 Pu) - \rho u \frac{GM_o}{r^2} + S(r)$$

where S(r) is an energy source or sink term. The corona is assumed to be a neutral electron proton gas so that

$$\rho = n(m_p + m_e) = nm \qquad (3.4)$$

where m_p and m are the proton mass and m_e the mass of the electron. For equal electron and proton temperature the pressure is given by

$$P = 2nkT. \qquad (3.5)$$

Parker further simplified the problem by assuming that the pressure and temperature were related by the polytropic law

$$P = P_o \left(\frac{\rho}{\rho_o} \right)^\alpha \qquad (3.6)$$

where α is the polytropic index. An isothermal gas corresponds to $\alpha = 1$ and an adiabatic process to $\alpha = 5/3$. The assumption of the polytropic law effectively assumes a solution to the energy conservation equation with an implied source term. Parker examined the solutions of the equations for a range of selections for α. See Parker [1963] or Hundhausen [1972] for further discussion and details.

The simplest case, but one that illustrates important points concerning the behavior of the solutions, is that of the isothermal corona. Near the sun the isothermal assumption is probably valid. Using the expressions for the density and the polytrope law with $\alpha = 1$, the momentum conservation equation becomes

$$nmu \frac{du}{dr} = -2kT \frac{dn}{dr} - \frac{nmGM_o}{r^2}. \qquad (3.7)$$

Equation (3.1) for mass conservation is integrated to give

$$4\pi nur^2 = \text{constant}, \qquad (3.8)$$

that is, the flux through a sun centered sphere is a constant. Equation (3.8) can be used to eliminate the number density from Equation (3.7)

$$\frac{1}{u} \frac{du}{dr} \left(u^2 - 2 \frac{kT}{m} \right) = \frac{4kT}{mr} - \frac{GM_o}{r^2}. \qquad (3.9)$$

Assume that the temperature of the corona is such that

$$T < \frac{GM}{r_o} \frac{m}{4k},$$

where r_o is the base of the corona. The right hand side of Equation (3.9) is negative in the range of $r_o < r < r_c$ where

$$r_c = \frac{GM_o m}{4kT}, \qquad (3.10)$$

and r_c is called the "critical radius." For $r > r_c$, the right hand side of Equation (3.9) will be positive. For $r = r_c$, the right hand side must be zero. In that case, to make the left hand side zero either

$$u^2(r_c) = \frac{2kT}{m} \qquad (3.11a)$$

or

$$\left. \frac{1}{u} \frac{du}{dr} \right|_{r = r_c} = 0. \qquad (3.11b)$$

These two conditions expressed in Equation (3.11a and b) define four classes of solutions to the set of simultaneous equations governing the model corona. If Equation (3.11a) is satisfied then du/dr has the same sign for all r, that is, u either increases or decreases monotonically with distance from the sun. If Equation (3.11b) is satisifed, then u is
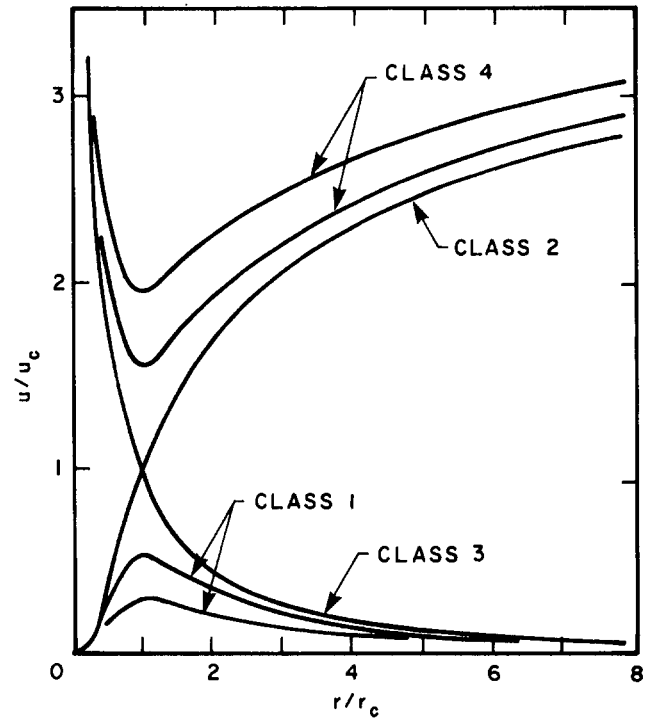

Figure 3-1. Topology of solutions to the solar wind equations for the spherically symmetric isothermal case. The only solution that can satisfy the boundary conditions of low velocity at the sun and low pressure at large distances is the class 2 solution [Hundhausen, 1972].

either maximum or minimum near r_c. These four classes of solutions for the velocity are shown in Figure 3-1. The physical solutions for the solar wind are members of the class of solutions that satisfy the physically relevant boundary conditions. Class 1 solution velocities approach zero near the sun and at great distances. Class 2 is the unique solution that has a low velocity near the sun, passes through the critical point, and has high velocity at great distances. Both class 3 and 4 solutions have high velocity near the sun. Class 3 is the unique solution passing through the critical point and having low velocity at great distances, whereas class 4 solutions have high distant velocities. Since, for the physical solutions, the velocity near the sun is small, class 3 and 4 solutions are immediately eliminated. Class 1 solutions would give finite pressures at large distances and would result in the same problem of matching to the interstellar medium as did the hydrostatic corona. For class 2, however, it can be shown that the expansion speed continues to increase slowly as $r \to \infty$, so that the density and hence the pressure approach zero at infinity. Thus the class 2 solution satisfies the boundary conditions and represents the physically existing solar wind. Since according to Equation (3.11a) the velocity at r_c is equal to the velocity of sound, this solution is supersonic for $r > r_c$.

Although the dicussion above is highly simplified [fol-

lowing Hundhausen, 1972] the essential characteristics are maintained in all more sophisticated treatments. That is, a family of solutions in every treatment exists but the imposition of the boundary conditions selects a finite number of solutions that have low velocities at the sun, pass through critical points where the flow becomes supersonic, and result in a high finite velocity and zero pressure at infinity.

The configuration of the solar wind magnetic field was also treated by Parker [1963]. Since the conductivity of the solar wind is extremely high, there is essentially no diffusion of the plasma transverse to the magnetic field and the field is said to be "frozen in" to the flow. The plasma carries the field with it into space. If the sun were not rotating, the field would extend straight outward in all directions but the rotation causes the field to appear wound up as shown in Figure 3-2. In a spherical system of coordinates (r, ϕ, θ)
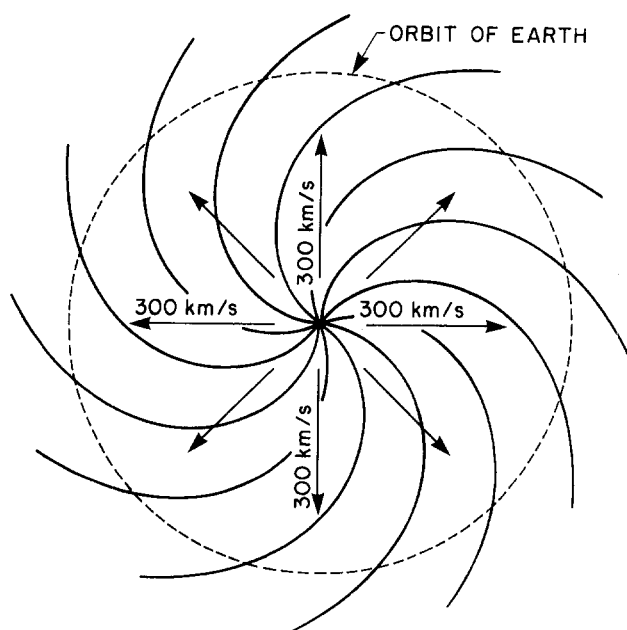

Figure 3-2. The configuration of the interplanetary magnetic field in the equatorial plane for a steady solar wind. The field winds up because of the rotation of the sun. Fields in low speed wind will be more wound up than those in high speed wind [Parker, 1963]. (Reprinted with permission from J. Wiley and Sons © 1963.)

rotating with the sun, the velocity of a fluid element carrying the field is given by

$$U_r = u$$
$$U_\phi = -\omega r \sin\theta \qquad (3.12)$$
$$U_\theta = 0$$

where u is the speed of the wind and ω is the angular velocity of solar rotation ($\omega = 2.7 \times 10^{-6}$ rad/s).

The velocity of the wind changes only slowly with radius beyond a few times the critical radius and will be approximated by a constant. The path followed by the fluid element is determined by

$$\frac{1}{r}\frac{dr}{d\phi} = \frac{U_r}{U_\phi} = \frac{u}{-\omega r \sin\phi}. \qquad (3.13)$$

For constant u beyond r_o this is integrated to give

$$r - r_o = \frac{-u}{\omega \sin\theta}(\phi - \phi_o) \qquad (3.14)$$

Then for a spherically symmetric geometry $\nabla \cdot \mathbf{B} = 0$ gives

$$B_r (r, \phi, \theta) = B (r_o, \phi_o, \theta) \left(\frac{r_o}{r}\right)^2$$

$$B_\phi (r, \phi, \theta) = -B (r_o, \phi_o, \theta) \frac{\omega r_o^2}{ur} \sin\theta \qquad (3.15)$$

$$B_\theta = 0.$$

The configuration near the solar equatorial plane is shown in Figure 3-2.

Transforming to a stationary coordinate system leaves the magnetic field configuration unchanged but in the stationary system there is an electric field

$$\mathbf{E} = -\mathbf{u} \times \mathbf{B} \qquad (3.16)$$

so that the direction of the plasma flow is radial rather than along the field lines.

3.1.2 Further Considerations

This simple spherically symmetric solar wind theory was remarkably successful in predicting the existence of the wind and estimating the velocity and density. However, it soon became apparent that the predicted velocity was lower than that observed and the predicted density was too large. Refinements of solar wind theory have taken many approaches, none of them as yet completely successful. The earliest attempt at improvement was to consider the electrons and protons as two fluids each expanding separately from the sun. The particles within each fluid were interacting with each other through large scale electric fields. This two-fluid model produced results that were again too slow and too dense, and the predicted total energy flux at 1 AU was twice that observed. Later, observations showed that the solar wind came from restricted areas of the sun so that the expansion of the wind was faster than the r^2 appropriate to the

spherical case discussed by Parker [1963]. Studies of the effect of this geometrical difference, however, showed that although the acceleration of the solar wind at small distances from the sun was increased markedly, the speed at 1 AU was not raised appreciably. A possible cause for the speed of the wind being higher than expected from simple theory is the effect of magnetohydrodynamic waves on the wind in the supersonic region. Theory indicates these waves will exert a force on the solar wind tending to accelerate it. At 1 AU, outward propagating Alfvén waves (Section 3.2.5) are the predominant mode observed. Fast mode MHD waves (Section 3.2.5) propagating outward near the sun would also accelerate the wind. Since this latter mode is strongly damped, it is quite reasonable that if there was a wave flux near the sun it would be lost before the wind propagated to 1 AU. This consideration is important because fast mode MHD waves are rarely seen at 1 AU. For both these wave acceleration mechanisms, an important problem is that the existence of the required waves in the required region has not been demonstrated. An alternative idea for wind acceleration is that the electron thermal conductivity has been overestimated by using the classical values, and at the same time, the thermal coupling between the electrons and protons has been underestimated. As with several other proposals listed here, this seems to be an attractive possibility but the observations and analysis have not been carried far enough to make a definitive test.

3.2 PARTICLE AND FIELD OBSERVATIONS

3.2.1 Coordinates

There are two coordinate systems commonly used to describe observations of the interplanetary medium [Russell, 1971]: geocentric solar ecliptic (GSE) and the geocentric solar magnetospheric (GSM). In the GSE system, X points from the earth towards the sun, Y is in the ecliptic plane and negative in the direction of planetary motion, and Z is parallel to the ecliptic pole. In GSM, X is along the earth sun line and positive in the direction of the sun, Z is positive toward the north and is perpendicular to X and in the plane which contains X and the earth's magnetic dipole axis, and Y completes the right handed system of coordinates.

GSM coordinates are usually used to describe interactions between the solar wind and the earth's magnetic field whereas GSE coordinates are used to describe the undisturbed solar wind. A second system sometimes used for the undisturbed solar wind is the geocentric solar equatorial system in which the X axis remains in the ecliptic plane pointing from the earth to the sun, but Y is parallel to the sun's equatorial plane and Z completes the system. The sun's pole of rotation is tipped at 7° to the plane of the

ecliptic. The transformations among the systems are given in Russell [1971].

3.2.2 Magnetic Fields

Observations of the magnetic field in the vicinity of the earth show that the field is, on the average, in the spiral direction predicted by the steady state model but that there are often large variations. The variations are ascribed to several sources: waves, discontinuities, and certain large scale disturbances. These topics will be described in Section 3.3. Here the basic large scale structure and average properties will be described.

The magnetic field in the solar wind is, as expected, drawn out in a spiral such that the angle the field makes with the earth-sun line is a function of the velocity, low solar wind speeds resulting in a tight spiral and faster speeds in a more radially aligned field. The angle increases with distance from the sun. For the observed velocities of the solar wind, the magnetic field has a spiral angle of about 45° at the earth. The magnitude of the field is on the order of a few nanotesla (earlier literature used the term gamma, $1\gamma = 1$ nanotesla). An example of observed magnetic field distributions is given in Figure 3-3a, b, and c [Hirshberg, 1969]. The direction of the radial component (often referred to as the x component) is, of course, either towards or away from the sun. Wilcox and Ness [1965] found that the field typically maintains one of these orientations for many days and then rapidly changes to the other. The region of space in which an orientation is maintained is called a "sector". The sector orientation is usually determined on the basis of one-hour or three-hour averages of the radial field component, but the maintenance of the sign of B_x is typically seen on a smaller time scale. Transitions from one sector to another take place over a period of minutes or hours. At transitions the direction of the interplanetary field usually changes sign rapidly while maintaining more or less the same magnitude. Sometimes the sector boundary on the scale of minutes or tens of minutes displays only a single change of sign. Sometimes the sign changes back and forth many times and over many hours before the field settles down to the new orientation. When this happens the position of the boundary may be hard to define. An example of the observed structure is shown in Figure 3-4. Typically, two or four sectors occur during a solar rotation. The sector structure can also be inferred from high latitude surface magnetic variations [Svalgaard, 1973]. The accuracy of the procedure varies with season and station latitude. The sector structure is stable over many months during the declining phase of the solar cycle, but changes from month to month during the increasing phase. The sector structures and/or the high speed streams (Section 3.3.2) apparently order a large amount of solar wind phenomenology. Studies of the typical behavior of the interplanetary medium within sectors
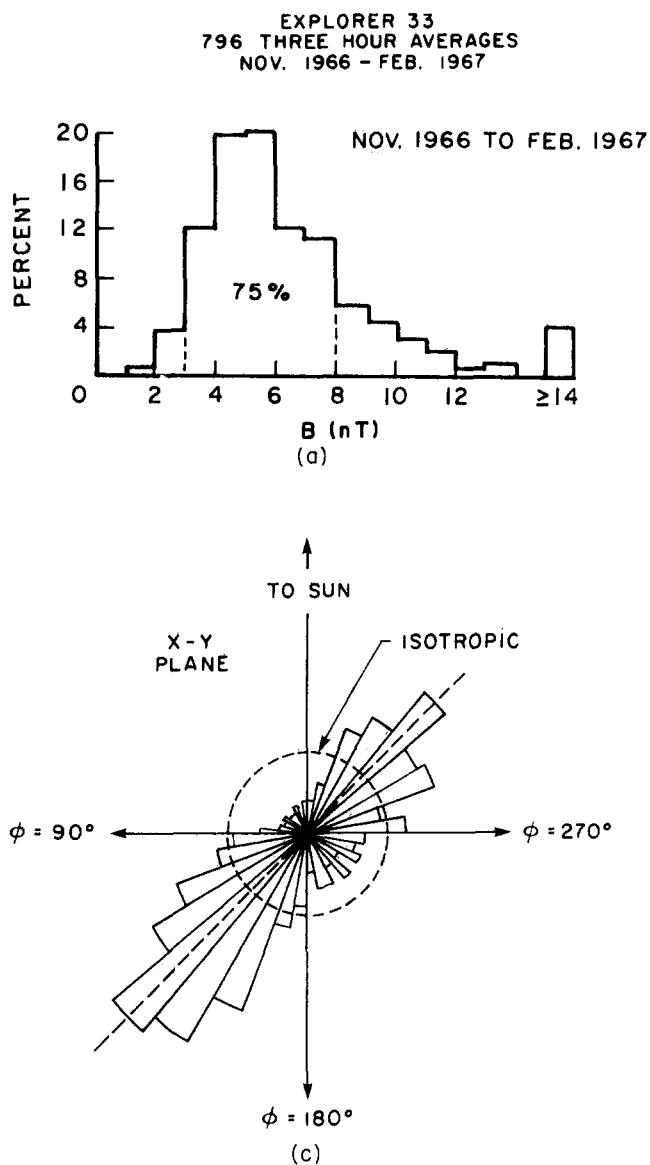
Figure 3-3. Observations of the interplanetary magnetic field. In this typical sample (a) the most common field magnitude is about 5 nT (1 γ = 1 nT) but the average of the magnitudes is higher because the distribution is skewed. (b) and (c) show the relative frequencies of the directions of the field. It tends to lie along the spiral direction appropriate to a velocity of about 450 km/s (i.e., about 45°) and in the solar equatorial plane but there are significant deviations [adapted from Hirshberg, 1969].

are relatively simple to carry out using sector boundaries as convenient time markers. The results of some of these studies are described in Section 3.3 on large scale disturbances.

Observations from spacecraft that traveled to solar latitudes of over 10° from the solar equatorial plane showed that the sector structure was dependent on latitude. The structure tends to disappear at higher latitudes, and the interplanetary magnetic field then has the sign of the solar magnetic field of the appropriate solar pole. The picture that has developed to explain these observations is shown in Figure 3-5. Plasma leaves the sun predominantly at high latitudes and flows out and towards the equator where a current sheet is formed corresponding to the change in magnetic field polarity. The current sheet is tipped relative to the sun's plane of rotation and warped so that as the sun rotates the earth passes through the current sheet, experiencing periods of alternating polarities, that is, sectors.

In the vicinity of the earth a typical magnetic field intensity $|B|$ is about 6 nT, but hourly average values vary from about 1 nT to a high of 37 nT. The highest recorded single value was 170 nT observed on 4 August 1972 [Burlaga and King, 1979]. Figure 3-6 shows the distribution of over 70 000 hourly values collected from satellites at 1 AU between 1963 and 1977. The distribution of the magnitude $|B|$ is skewed towards high values. However, the distribution of the log $|B|$ is distributed normally with a mean of 0.75 ($|B|$ = 5.6 nT) and an rms deviation of 0.18. For about 3% of these hours log $|B|$ exceeded the mean by at least 20, that is $|B| \geq 13$ nT. When the field is high it typically remains so for many hours, forming distinct events. There were about 100 such events observed between 1963 and 1974 of which 75% were associated with shocks or interfaces between interacting solar wind streams (Section 3.3.2). Periods of high-intensity field may persist for as long as 24
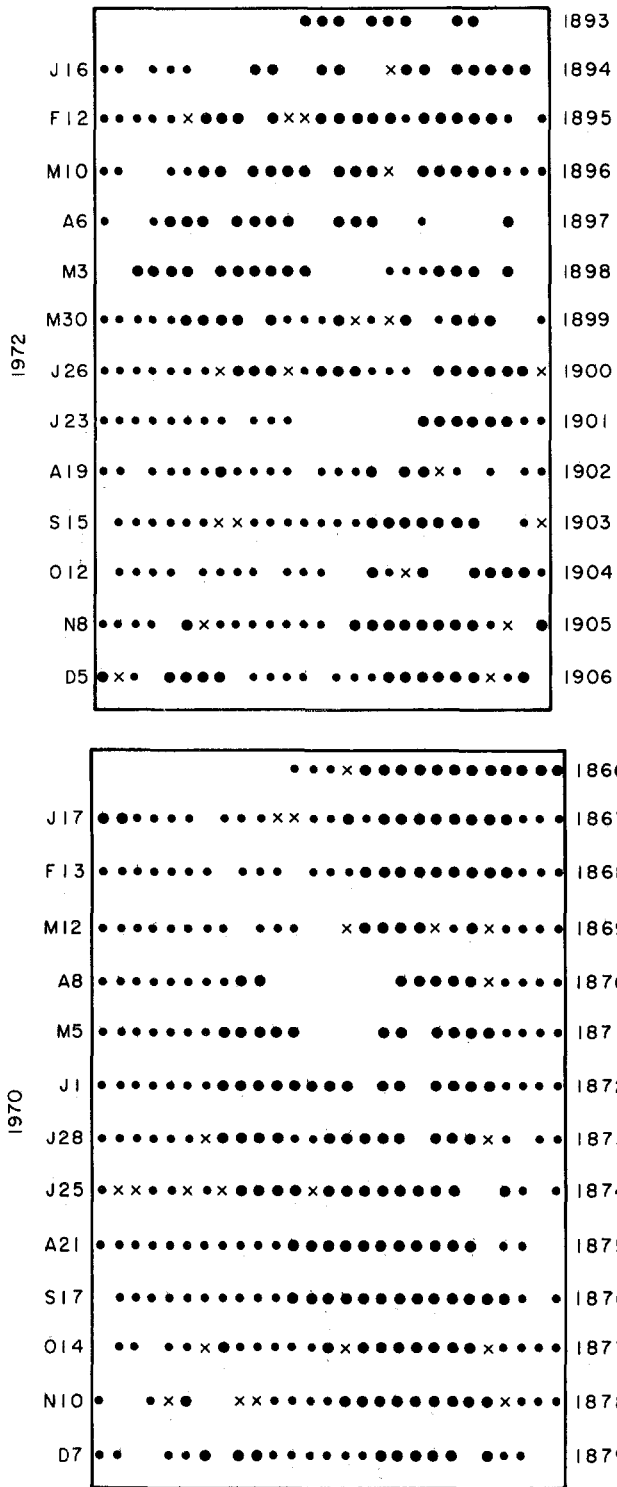
Figure 3-4. Two years of sector structure polarity. A small dot indicates a day with polarity directed away from the sun; a big dot, towards the sun; a cross, an ambiguous day; and a blank, a data gap. Each line represents one solar rotation or 27 days. The date of the first day of the rotation is given on the left-hand scale and the number of the rotation on the right-hand scale. Note the strong tendency for sector structure to repeat on subsequent rotations [adapted from Wilcox et al., 1975].
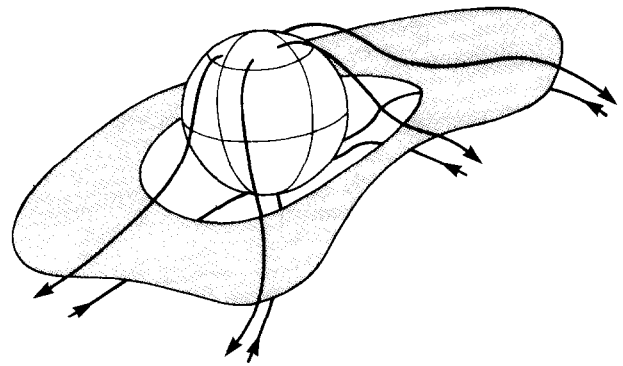

Figure 3-5. Sketch of the current sheet responsible for the sector structure. The sheet is warped and tilted relative to the plane of solar rotation [Smith, 1979].

hours. The persistence of a given level of |B| can be found from the autocorrelation function which falls to 0.5 at about a 15-hour lag [Burlaga and King, 1979].

An important magnetic field parameter is the component of the field perpendicular to the X-Y plane. This component, B_z, plays a central role in the coupling of the wind and the earth's magnetic field such that when B_z is southward and
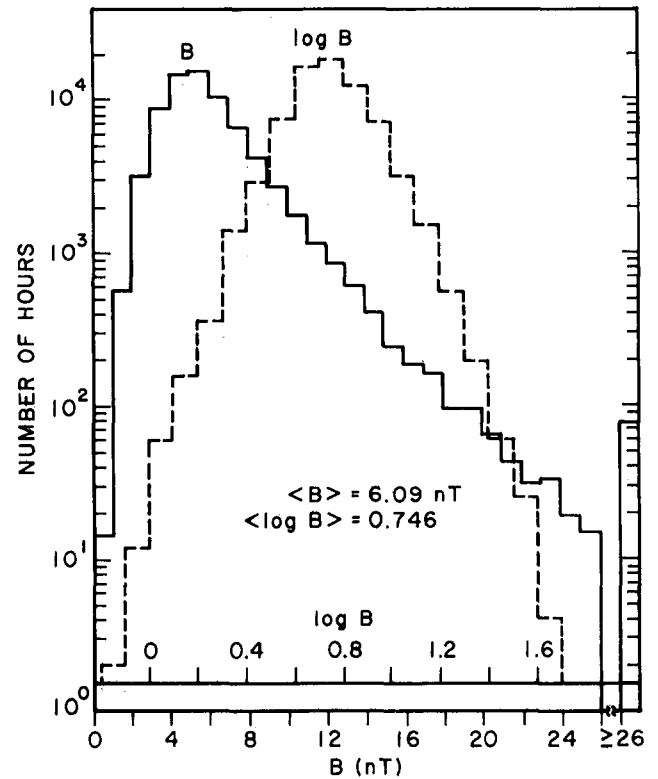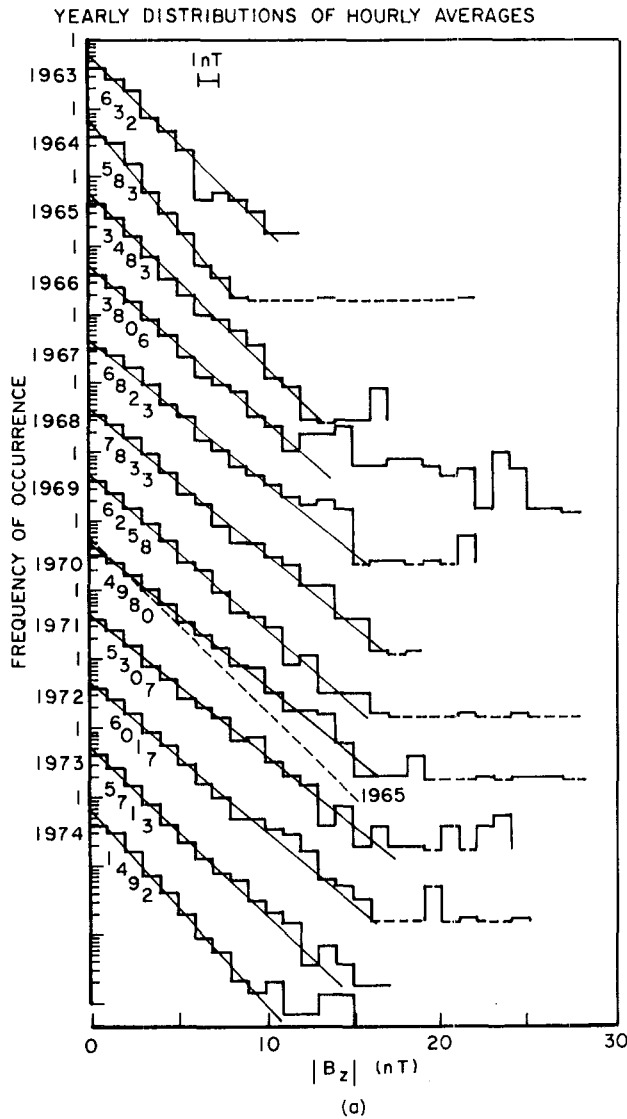

Figure 3-6. Distribution of 71431 hourly averaged values of the interplanetary magnetic field magnitude |B|, and of log |B|. These data were collected between 1963 and 1977. The average value of B is 6.09 nT but the average of log B corresponds to a value of 5.6 nT. The most common value of B is about 5 nT [Burlaga and King, 1979].

YEARLY DISTRIBUTIONS OF HOURLY AVERAGES

(a)

large, geomagnetic disturbances occur. Figure 3-7a shows distributions of GSE B_z observed for each year from 1963 to 1974 [Siscoe et al., 1978]. The figure gives the number of times $|B_z|$ fell within each 1 nT bin. The number of values used in each histogram is also given. The distributions are generally exponential, but with a high intensity tail. The exponent changes in a systematic way with the solar cycle. These data are collected in Figure 3-7b which gives the probability that an hour chosen at random from the set of over 50 000 hours of observation will fall in a particular 1 nT bin. Of course, a figure of this type made using different years of observation would differ somewhat from that shown. The finding that the most probable value of B_z is less than 1 nT is in general agreement with the notion that a steady spherically expanding solar wind would have no B_z component when measured in the sun's equatorial plane. The B_z component is primarily due to disturbances such as waves or interacting parcels of the interplanetary medium.

3.2.3 Protons and Electrons

The solar wind plasma consists of protons, doubly charged helium ions, a small number of other positively charged particles, and enough electrons so that the plasma is electrically neutral. The Debye length is about 10 m. Since commonly 95% of the positively charged particles are protons, it is the protons that are usually referred to when statements are made about the solar wind bulk properties such as velocity, density, and temperature. In this section the large scale general properties of the wind will be described for protons and electrons. Alpha particles and heavy ions will be dealt with in Section 3.2.4.
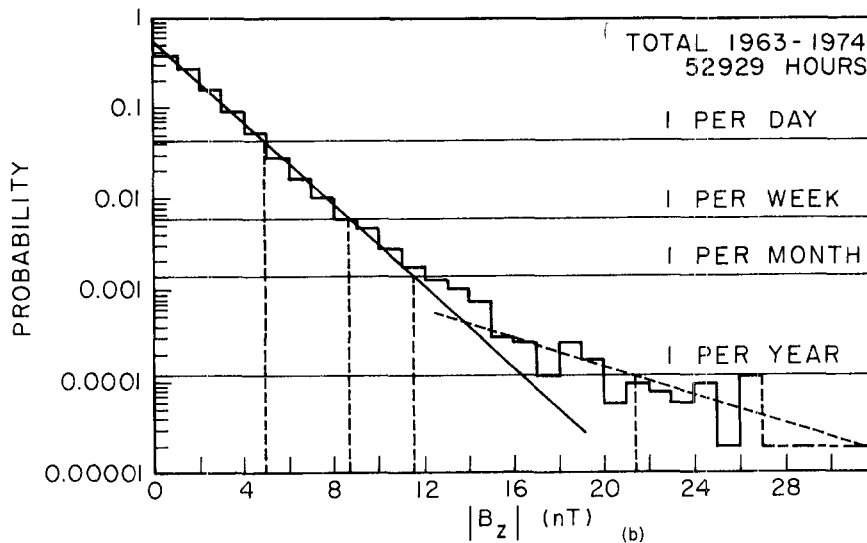

(b)

Figure 3-7. (a) The distributions of the magnitude of the hourly average value of the component of the interplanetary magnetic field perpendicular to the ecliptic plane, $|B_z|$. Data for each year from 1963 to 1974 are plotted. The data coverage varied from year to year. Note the changes in slope and the high intensity tail. (b) Histogram of the occurrence frequency of $|B_z|$ based on the 52 929 values used in the above distributions. The ordinate gives the probability that an entry selected at random will fall in the particular 1 γ bin. Levels for selected average recurrence periods are marked. For example, the average time between observations of $13\gamma > B_z \geqslant 12\gamma$ is about one month [Siscoe et al., 1978].

3-7

CHAPTER 3

Solar wind properties do not vary randomly on a time scale of hours. Instead the wind is organized mainly into periods of slow plasma and fast plasma, with the slow and fast regions interacting. The structure of these streams will be discussed in Section 3.3.2. Here the interest will focus on typical values of physical parameters.

Early plasma probes detected protons and other positively charged particles but did not permit detailed descriptions of particle distributions to be made. However, the first three moments of the distribution could be determined, that is, the proton velocity, density, and (less exactly) the temperature. A typical distribution of speeds is shown in Figure 3-8. The direction of flow is almost always from the sun
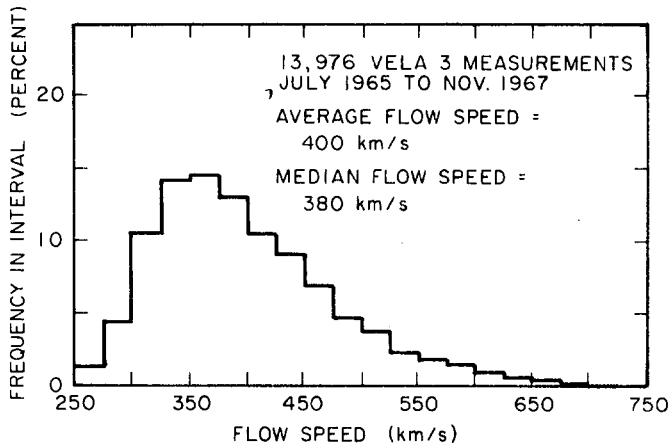

Figure 3-8. A frequency distribution of solar wind speed [Hundhausen, 1972]. Both the average speed and the shape of the distribution differ from year to year.

(within a few degrees). The major causes of non-radial flow are aberration and interaction of fast and slow solar wind structures. The amount of deviation from radial flow due to the angular velocity of the source of the solar wind at the sun is still a matter of debate. Although there is considerable variation in the velocity distributions for different time periods, they all have nearly the same range of values. In Figure 3-8 there are few measurements with velocities lower than 275 km/s and in data sets from several other years there were none. In the sample shown, values higher than 650 km/s were rare but in other years the upper frequency bin with non-negligible sample number was 775 km/s. Velocities of over 1000 km/s occasionally have been reported after extremely energetic flares occurred on the sun. Autocorrelation among speed measurements is high for lags of less than 40 h, reflecting the stream structure (Section 3.3.2). Table 3-1 shows average values and ranges for 3-hour average speeds for about 3.5 years of data [Feldman et al., 1977]. The average velocity given there is 468 km/s, somewhat higher than that shown in Figure 3-8.

The density of the proton component is also ordered by the fast and slow velocity streams with an average of 8.7

particles/cm^3. Most of the extreme density values are due to rarefaction and compression arising through stream interactions or solar flare disturbances discussed in Section 3.3.3. The proton temperature T_P, which increases with the velocity, varies by a factor of twenty and has an average of 1.2×10^5 in this data set.

The proton distribution function varies widely and is usually not well represented by a single Maxwellian. Figures 3-9a and b show examples of two-dimensional proton velocity distributions. Figure 3-9a shows a simple distribution with a single peak, corresponding to a single velocity and density. Figure 3-9b shows a distribution with a strong second peak corresponding to a plasma having two beams with different velocities and densities. The most usual distribution is between these two and would show a single major peak with evidence for a high velocity tail. Note that in both main peaks the spread in contours is greater in one direction than at right angles, that is, the temperatures parallel and perpendicular to some direction (the direction of the magnetic field) are not equal and are often given separately. The temperature T_p is $1/3$ ($T_\parallel + 2T_\perp$) where $\parallel$ and $\perp$ denote components parallel and perpendicular to the magnetic field. The average value of $T_\parallel/T_\perp$ is 1.5 with a range of 0.7 to 2.8. Distributions that have two velocity peaks can be described as two streams of protons moving relative to one another. The higher density streams are usually the lower velocity ones.

Solar wind electrons are more difficult to observe and their properties have been described less fully than those of the protons. In contrast to protons, electrons are subsonic at earth. Observed distributions of electrons are shown in Figure 3-10 [Feldman et al., 1975]. Note that because of the subsonic velocity, the spreads in particle speeds are much larger than the bulk speed. Very low velocity electrons, which would allow an actual measurement of the bulk speed to be made, cannot be measured at all because of observational difficulties. The figure shows four cuts through the distribution. Figure 3-10a shows particle fluxes in the direction parallel and anti-parallel to the electron heat flux. Since the electron heat flux is along the magnetic field direction these two cuts are also in directions parallel and anti-parallel to the magnetic field. Note that fluxes for each speed are not the same in two directions, indicating that a substantial heat flux is carried by the electrons. In fact, it is the electrons that regulate the heat flux in the wind as a whole. The curves in the upper panel represent fits to the points, the fits to the lower speeds being Maxwellians. Note that although the two Maxwellians are excellent fits at low speeds, they fail decisively at high speeds. In much of the data reported in the literature, the higher speed particles are fit with a second set of two Maxwellians or a somewhat more complex function as shown here. In Figure 3-10b the data shown are from a plane perpendicular to the heat flux. Two data sets are shown: one for positive and one for negative directions along a line in the plane. The fluxes are the

Table 3-1. Average solar wind parameters

Parameter	Mean	σ	5–95% Range Limit
speed (km/s)	468	116	320 to 710
density (proton/cm^3)	8.7	6.6	3.2 to 20
M_A	10.7	4.8	4.4 to 20
M_S	7.7	1.5	5.6 to 10
$|B|$ (nT)	6.6	2.9	2.2 to 9.9
T_p (K)	1.2×10^5	9×10^4	1×10^4 to 3×10^5
T_e (K)	1.4×10^5	4×10^4	9×10^4 to 2×10^5
T_e/T_p	1.9	1.6	0.37 to 5.0
n_α/n_p	0.047	0.019	0.017 to 0.078
T_α (K)	5.8×10^5	5×10^5	6×10^4 to 15.5×10^5
T_α/T_p	4.9	1.8	2.3 to 7.5
β_p	0.7	0.9	0.11 to 1.7
β_e	1.3	1.9	0.3 to 3.1
$\beta_p + \beta_e$	2.1	2.4	0.5 to 4.6
C_A(km/s)	50	24	30 to 100
C_S(km/s)	63	15	41 to 91

(Information from Feldman et al.,[1977])

same in these two directions showing that the electron distribution function is symmetric about the magnetic field direction. Again the data are fit with Maxwellians at low speeds and more complex functions are fit to the residual fluxes at high speeds. The low speed portions of electron distribution functions are collision dominated, whereas the very high speed portions are collisionless. Observed distribution functions are consistent with a theoretical model in which the entire distribution at all velocities arises from the effects of Coulomb collisions [Scudder and Olbert, 1979].

Although there is not yet general agreement concerning the best method for describing and interpreting electron observations, the data presentation that is used here is that of Feldman et al. [1977], in which the measured flux distribution is broken up into low and high speed parts as shown in Figure 3-10. The electron and proton densities and bulk velocities are set equal, consistent with the observations. The electron distribution function is described as a superposition of two distributions, one a cold component f_c and the other a hot component f_h, so that $f = f_c + f_h$. The cold component electrons below 50 eV that can be well fit with a bimaxwellian function are also known as the core electrons. The hot component or halo electron component is defined as the remainder of the measured distribution function after the cold component is subtracted. In this scheme from 3 to 10% of the electrons belong to the hot component. The energy at which f_h begins to rise above f_c is about 60 eV. The hot and cold components generally move relative to one another along the magnetic field direction so that no net current flows in the frame of reference moving with the protons. The total bulk velocity is observed to be within about 50 km/s of the proton velocity. The total heat flux in the solar wind is primarily carried by the hot electron component. If both halo and core components are fit with bimaxwellian distributions then the average core electron temperature is 1.2×10^5 K, whereas the average halo electron temperature is 6.9×10^5 K. The value of 1.4×10^5 K given in Table 3-1 is the temperature derived from the fit of the distribution function as a whole. As can be seen from Table 3-1, the electron temperature does not vary as widely
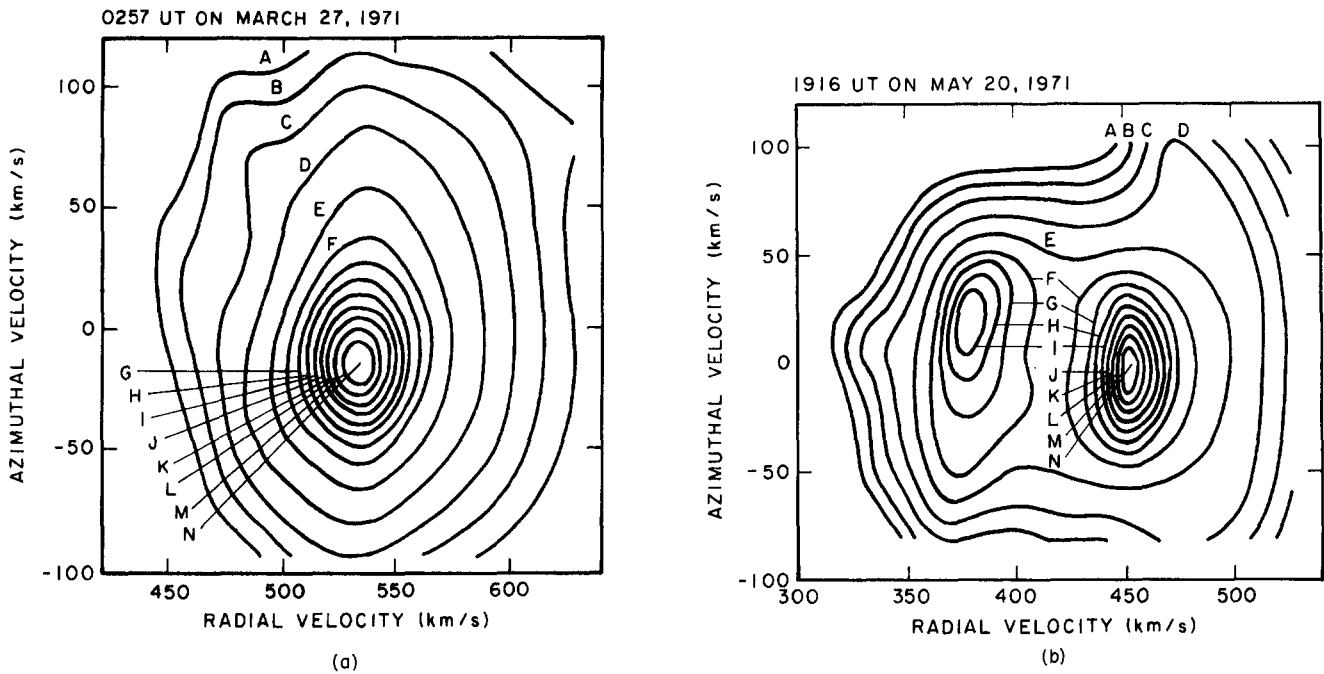
Figure 3-9. Proton velocity distributions. Two examples (a,b) of two-dimensional proton velocity distributions contoured for equal number density. Contours A, B, C and D correspond to 0.001, 0.0032, 0.01 and 0.032 and contours E through N to 0.1 to 1.0 in steps of 0.1 of the peak contribution to the proton number density [Feldman et al., 1974].
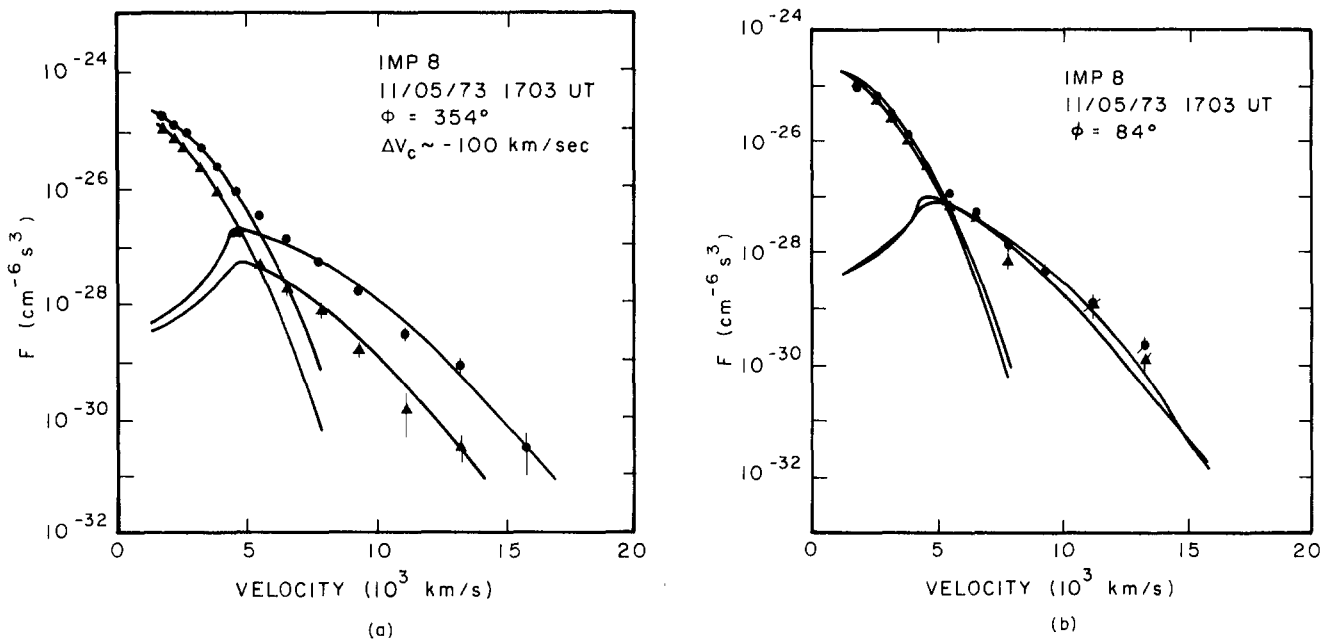

Figure 3-10. Electron flux as a function of speed [Feldman et al., 1975]. (a) shows the flux parallel and anti-parallel to the direction of the electron heat flux. (b) shows the fluxes in a perpendicular plane.

as the proton temperature. The electron thermal pressure is usually, but not always, greater than the magnetic field pressure ($\beta = 8\pi nkT/B^2$, $\beta_e > 1$). Thus, although the proton thermal pressure is usually less than the magnetic field pressure ($\beta_p < 1$), the average β calculated using the total thermal pressure is about 2 (Table 3-1).

3.2.4 Other Ions

Since helium is the second most abundant solar constituent, it was expected to be present in the solar wind in quantities that could be detected by the early solar wind probes. This expectation was fulfilled with the flight of Mariner II in 1962 [Neugebauer and Snyder, 1966]. However, the measured values of the abundance, velocity, and temperature of the helium component of the wind were so different from what would be expected on the basis of simple theory that the behavior of helium is still not well understood. For a recent review of helium observations see Neugebauer [1981]. Observationally, the helium properties are ordered by large scale structures such as sectors, velocity streams, and flare disturbances. These properties will be discussed further in Section 3.3. The simplest helium parameters to measure are relative abundance, velocity, and temperature. The major unexpected results are that in the vicinity of the earth, relative abundances of helium by number, n_α/n_p, vary from less than 10^{-3} to more than 0.3, helium velocities tend to be a few km/s larger than hydrogen velocities, and the temperature of helium is usually about 3 or 4 times that of hydrogen.

Helium in the solar wind is almost always completely doubly ionized, as would be expected because of the high coronal electron temperatures. However, a few events have been reported in which He^+/He^{++} reached levels as high as 0.1 [Schwenn et al., 1980] and 0.3 [Gosling et al., 1980]. These events have been interpreted as the inclusion into the wind of material from relatively cool chromospheric prominences.

The distribution of relative abundance values of He^{++} by number measured by the Vela 3 satellites is shown in Figure 3-11 [Robbins et al., 1970]. For this data set the values ranged from 8.1×10^{-4} to 4.2×10^{-1}. The yearly average abundance between 1962 and 1976 varied from 3% to something over 5%. The helium abundances are not distributed randomly in the plasma but instead show systematic behavior that has not yet been satisfactorily explained theoretically. Most values of $n\alpha/np \geqslant 0.15$ in Figure 3-11 were observed in solar wind reliably associated with major solar flares [Hirshberg et al., 1972]. Although most helium abundance enhancements are associated with flares, regions of solar wind containing between 9% and 15% helium plasma are sometimes seen in low speed wind with no association with major flares or interplanetary shocks (Section 3.3.3). In general, the data suggest that unusually high solar wind

helium abundances may be associated with impulsive injections into the wind of hot or cool coronal plasma as a result of solar activity but there does not appear to be a one to one correlation. Helium abundance also shows a trend toward larger values in higher velocity winds but this trend is time dependent and may change with the solar cycle. The average abundances at velocities of 300 km/s vary between 3% and 4%, and at 500 km/s average abundances between 5% and 9% have been reported [Neugebauer, 1981].

The helium and hydrogen components of the solar wind have almost the same speed at 1 AU. However, differences of up to a few tens of kilometers are common, and the helium is usually moving faster than the hydrogen. The average reported value of the ratio of the helium to hydrogen speeds $\langle v_\alpha/v_p \rangle$ ranges from 1.001 to 1.035 and is always positive. The direction of helium motion relative to hydrogen is generally along the direction of the magnetic field. At 1 AU the velocity difference $v_\alpha - v_p$ is in general proportional to, but less than, the Alfvén wave speed. Also,
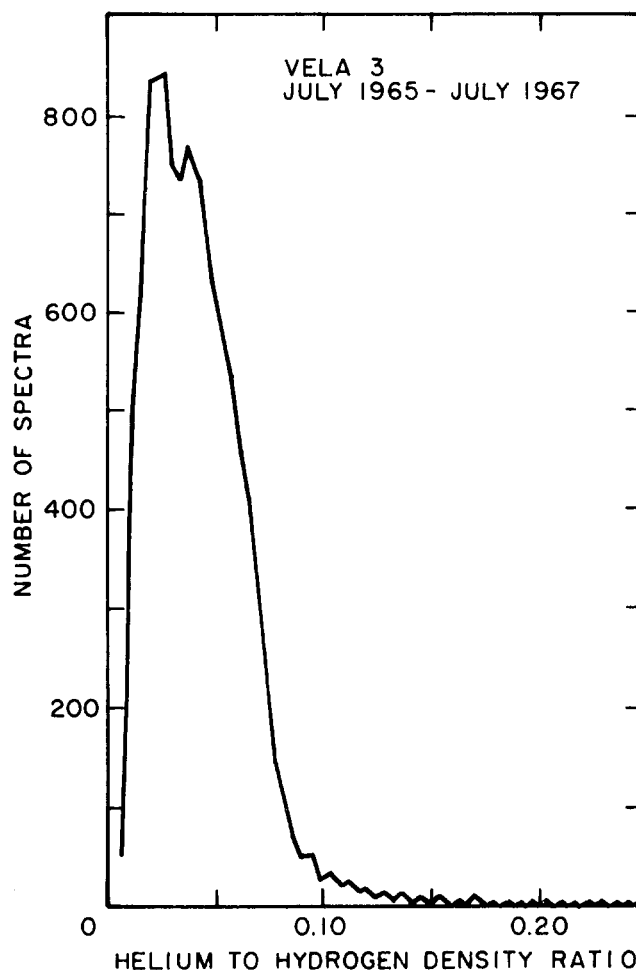

Figure 3-11. The distribution of solar wind helium to hydrogen number density ratios [Robbins et al., 1970]. The helium enhancement events reflected in the high abundance tail are often associated with major solar flares.

$v_\alpha - v_p$ is strongly dependent on the ratio of the solar wind expansion time to the Coulomb collision slowing down time. The expansion time scale is defined as the time required for a solar wind ion to move through one density scale height. It has been suggested that the helium is accelerated to higher velocities than hydrogen by waves in the interplanetary medium but as yet there is no direct observational confirmation.

The temperature of helium is almost always higher than that of hydrogen, and it appears that there is a tendency for the thermal velocities of the two components to be equal rather than for the temperatures to be equal. The most probable value of T_α/T_p is between 2 and 4 but values as high as 10 are occasionally observed. Average values of T_α/T_p calculated from different data sets have varied from about 3 to 5. It is not known if this difference is due to actual changes in the solar wind or to inaccuracies in the measurements. There is a positive correlation between T_α/T_p and $v_\alpha - v_p$. The behavior of T_α is not understood theoretically but it has been suggested that the waves that can preferentially accelerate helium may also heat the ions by an amount roughly proportional to their masses.

In addition to ^4He ions, solar wind ^3He ions have been detected. The $^4He^{++}/^3He^{++}$ ratio has been measured both from foils left on the lunar surface and directly using an ion composition experiment on ISEE 3. The results of the two techniques are in agreement. The ISEE experiment found on average $^4He^{++}/^3He^{++}$ of $2\cdot1 \pm 0.2 \times 10^3$ using more than 4000 observations; however, the distribution was very broad. Low ratios, which lasted a few hours, had a tendency to characterize periods of low $^4He^{++}$ flux [Ogilvie et al., 1980].

Some ions heavier than helium have been observed in the interplanetary medium. The observations are difficult to make because of the low ionic abundances. However, neon has been collected on foils on the moon, and plasma probes have been able to resolve oxygen, iron, and silicon at times when the plasma temperatures are low. The relative abundances are within a factor of ten of coronal abundances, and the speeds tend to be the same as the speeds of the helium observed at the same time. There does not appear to be any further acceleration of heavy ions. The temperatures however, apparently increase further with higher ion mass and measurements of oxygen temperatures suggest that the thermal speeds of all constituents tend to be equal in the solar wind [Ogilvie et al., 1980].

The ionization state of heavy ions provides important information on the electron temperature at their source in the corona. The ionization state of the atom in the collision dominated corona is determined by a balance between ionization by electron collisions and recombination due to radiative and dielectronic processes. As the solar wind moves away from the sun, collisions become more rare, and beyond some heliocentric distance the ionization state of the particle remains unchanged. This process, called "freezing in," permits the particles to be used as tracers of their sources. (Note that the term "freezing in" has already been used in

another context in Section 3.1.1. The two uses are so different they almost never cause confusion.) The heliocentric distance at which freezing in occurs depends somewhat on the type of particle involved because of the details of the interactions. In slow, low temperature regions of the wind the abundances of O^{6+} to O^{7+} ions in the available data set indicate a freezing in temperature of 2.1×10^6 K and the abundances of Fe^{7+} through Fe^{13+} yield 1.5×10^6 K. Other plasma, associated with solar wind accelerated by flares showed oxygen and iron freezing-in temperatures of 3×10^6 K [Bame et al., 1979], and iron charge states have indicated temperatures as high as 1.6×10^7 K.
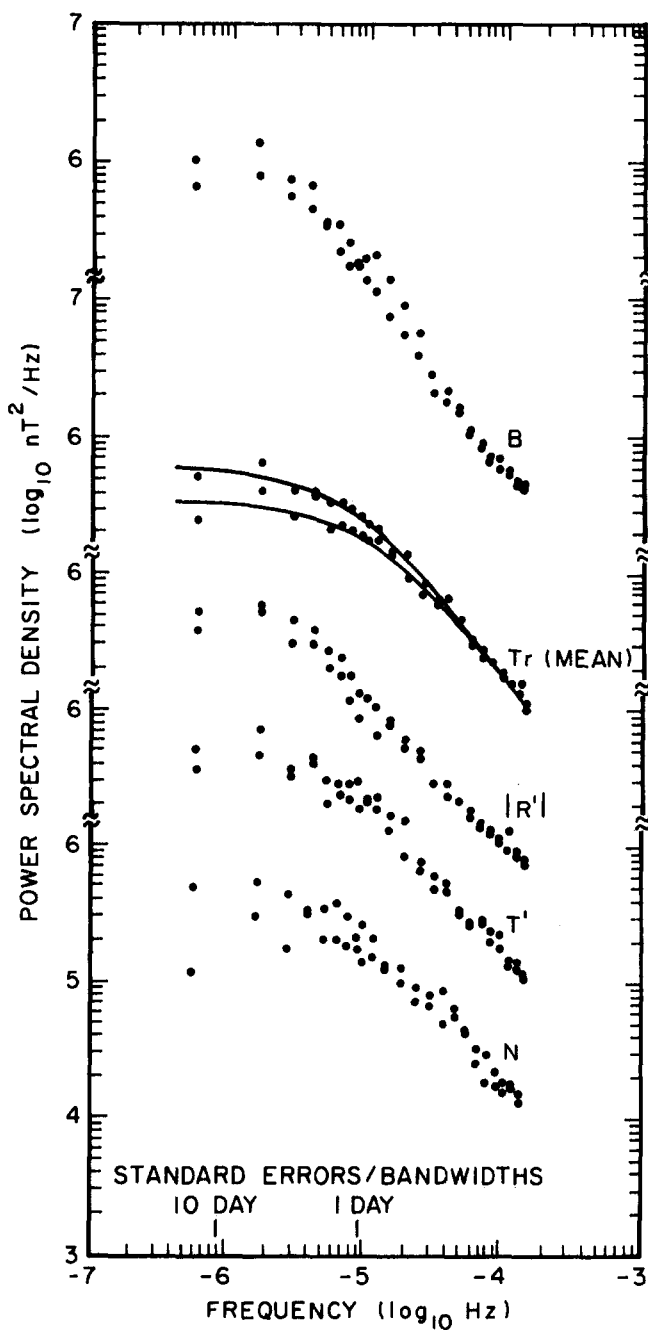
3.2.5 Waves and Turbulence

Observations of the solar wind show that there are variations in almost all quantities on all time scales. For example, as discussed in Section 3.2.2 the interplanetary magnetic field of a uniform undisturbed wind should not have any Z component; however, hourly average Z components are about 1/3 the intensity of the field magnitude. This Z component is due to the presence of waves and discontinuities in the plasma.

Considering the solar wind as a turbulent medium, power spectra have been calculated and compared with the theoretical predictions based on magnetohydrodynamic turbulence theory. Spectra of the magnetic field, particle density, and particle velocity variations have been given in the literature.

Magnetic field data lend themselves to these studies because of the good time resolution and accuracy of the measurements. Examples of spectra in the 10^{-7} to 10^{-1} Hz range are given in Figures 3-12a and 3-12b [Hedgecock, 1975]. If the field could be described as that ideally present in a spherically expanding constant velocity solar wind without fluctuations, there would be no components in the two transverse directions. The top curve in Figure 3-12a gives the power in the variations of magnitude. The power levels in the magnitude are much lower than the levels in the components. The spectra of the two transverse components (T and N) are very similar and have been averaged to produce the transverse spectrum Tr. A composite spectrum of the transverse power is shown in Figure 3-12b. Note the different spectral indices used to fit the data in the different frequency ranges. The magnetic field power spectrum for periods greater than a day tends to flatten. The power spectrum slope varies from day to day, or for lower frequencies from sample to sample. In the 10^{-5} to 10^{-3} Hz range both the slopes and the absolute value of the power variations are consistent with a factor of 10 variation, [Hedgecock, 1975]. When the spectrum was fitted with a line given by F, the average spectral exponent N for 17 periods in 1972 was 1.27.

Examples of power spectra of solar wind fluctuations in positive ion flux are shown in Figure 3-13a [Neugebauer,
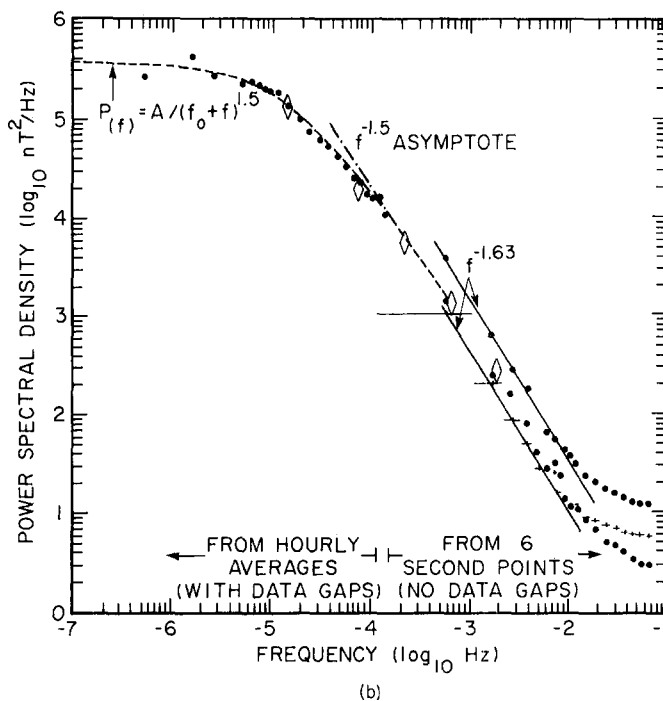
(a)

(b)

Figure 3-12. (a) Power spectral density (PSD) of the interplanetary magnetic field. The R direction is along the average spiral direction of the field, N is in the solar meridian plane and T completes the system. B is the magnitude of the field. The components are as marked. T_R is the average of the transverse (N, T) spectra [adapted from Hedgecock, 1975]. (b) A composite mean transverse power spectrum for 1972 [Hedgecock, 1975].

1975]. Curves A and D are for the noisiest and quietest 100 spectra of the 1728 spectra in the data set used in this study. In the 10 second region these two power densities differ by more than a factor of 100. Curves B and C are two different types of averages of the entire data set. In curve B the values of the power density are simply averaged. In curve C the logarithms of the power spectral density are averaged to avoid giving too much weight to the shape of the spectra from the most turbulent intervals. The error bars represent 90% uncertainty levels. The enhancement at high frequencies is probably due to fluctuations at the proton thermal

gyroradius. A long period velocity spectrum is shown in Figure 3-13b from Coleman [1968].

Frequently, fluctuations in the solar wind can be recognized as distinct types of waves and/or discontinuities. Discontinuities will be discussed in Section 3.3. Although a kinetic theory treatment is required for a proper description of the behavior of waves, the magnetohydrodynamic theory is useful for classifying the waves [Barnes, 1979]. There are three types of MHD waves, the transverse Alfvén (or intermediate) wave, and fast and slow magnetoacoustic waves. The transverse Alfvén wave is non-compressive with constant magnitude of the magnetic field, but not constant direction. The fluctuating magnetic field and velocity are related by

$$b = \pm (4\pi\rho)^{1/2}v \qquad (3.17)$$

where b is the magnetic perturbation, v is the velocity perturbation, and ρ is the constant density. The velocity of an Alfvén wave is given by $C_A = B/(4\pi\rho)^{1/2}$. Typical values of C_A are given in Table 3-2.

The two magnetoacoustic modes are compressive and their magnetic fluctuations are nearly linearly polarized. The velocities of the fast and slow waves are given by

3-13
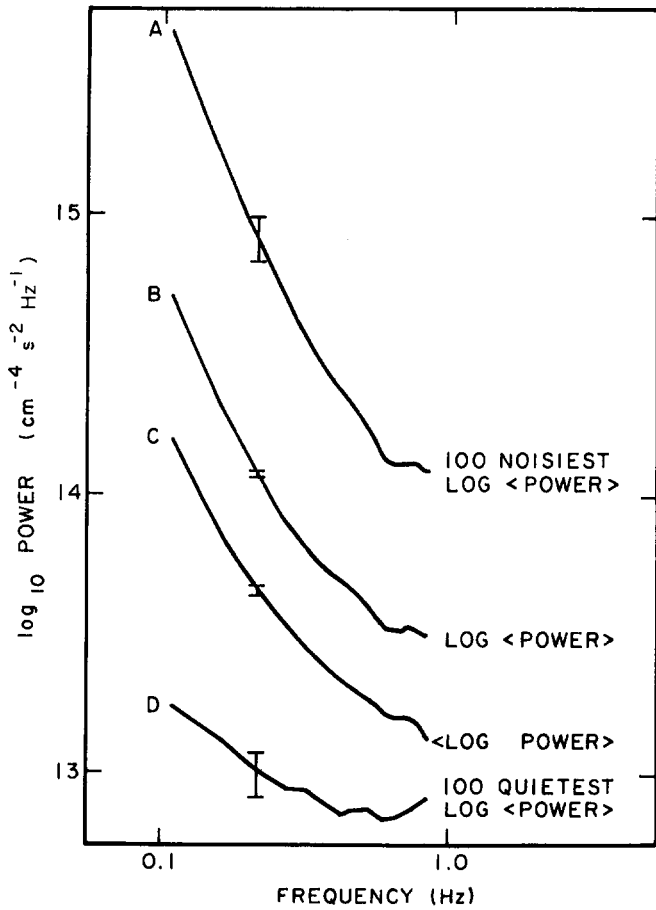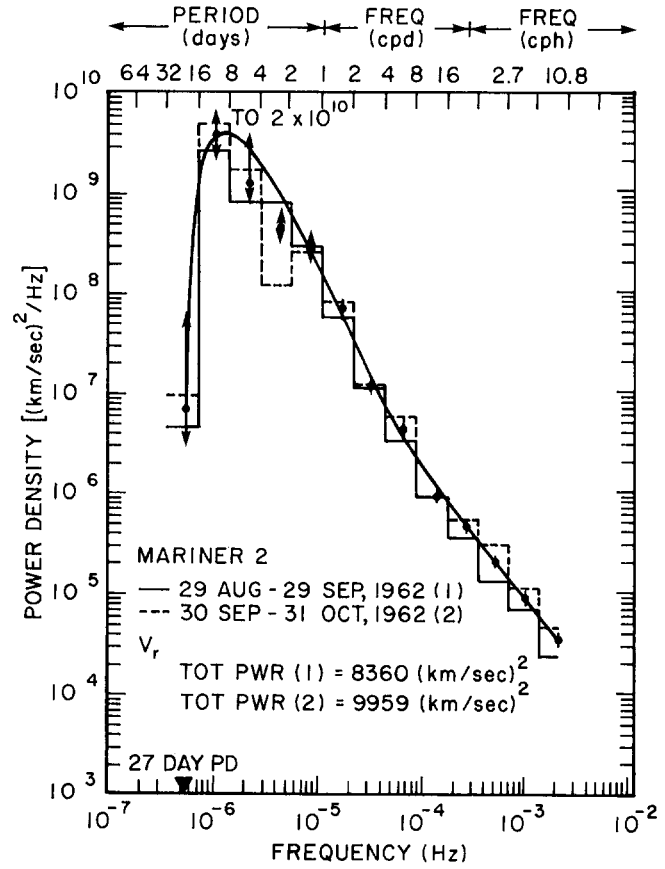
Figure 3-13. (a) Four different types of averages of the power spectral density of variations in the total charge flux of positive ions [Neugebauer, 1975]. (b) Power spectra of the solar wind velocity in 1962 [Coleman, 1968]. (Reprinted with permission from the American Astronomical Society © 1968.)

$$v_m = \frac{1}{2}\left[(C_A^2 + C_S^2) \pm \left(C_A^4 + C_S^4 - 2C_A^2 C_S^2 \cos 2\theta\right)^{1/2}\right] \qquad (3.18)$$

where C_S is the speed of sound, θ is the direction of the wave normal relative to the field, and the plus is taken for the fast mode and minus for the slow mode. Typical values of C_S are shown in Table 3-1 where $C_S = [k(T_e + 3T_p)/m]^{1/2}$. This expression assumes the electrons respond isothermally and the protons adiabatically to one dimensional sound waves as expected from the electrons role in heat conduction. In the limit of small amplitude waves, fluctuations can be thought of as a superposition of these three types of MHD waves. However, the waves in space are not small amplitude so that their behavior is more complex than described by small amplitude MHD theory. The magnetoacoustic modes will be damped and so will not be expected

to be observed far from their place of origin. The Alfvén wave, however, is not damped.

By far the most commonly observed wave in the solar wind is the Alfvén wave. An example is shown in Figure 3-14. In this figure R is the radial direction and N and T are transverse directions. The velocity and field component variations are approximately related according to the expression above. The magnetic field magnitude and the plasma density show very little variation. Interplanetary fluctuations are dominated by large amplitude aperiodic Alfvén waves more than 50% of the time [Belcher and Davis, 1971]. The clearest examples occur in high velocity streams (Section 3.3.2) and their leading edges. These waves are propagating outward in the rest frame which implies that they are produced in or near the sun below the critical point of the flow r_c. They have not yet been actually observed in the vicinity of the sun and this is a very difficult observation to make without in situ detectors. In the vicinity of the earth, changes in the magnitude of B are small with $\Delta|B|/|B| \sim 0.06$ whereas the variation of the components is relatively large with $\Delta B_i/|B| \sim 0.4$ where i indicates a component [Burlaga and Turner, 1976]. The direction of minimum variance of the field is
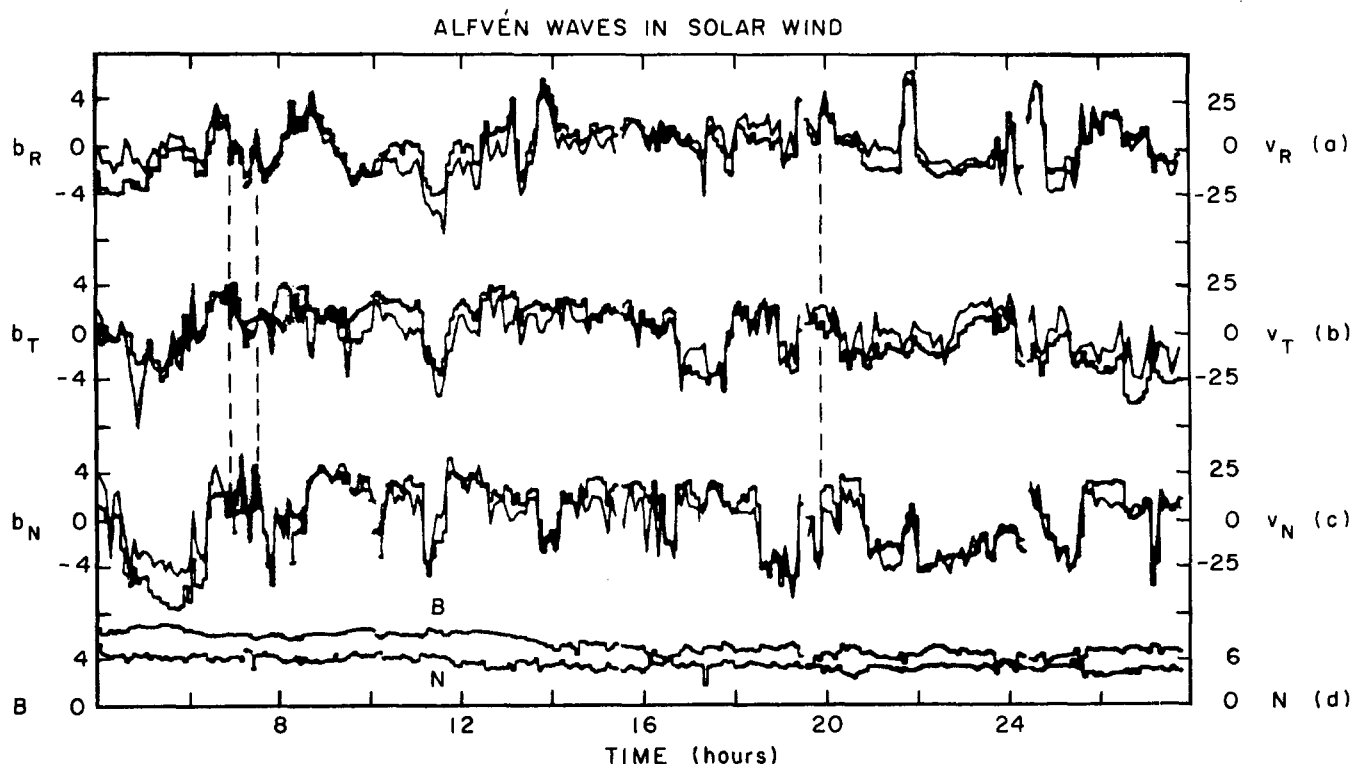
ALFVÉN WAVES IN SOLAR WIND

Figure 3-14. Alfvén waves in the solar wind. Curves a, b & c show that the strong variations of the magnetic field components occur simultaneously with like variations of the velocity. Curve d shows that the field magnitude and density were both very steady [Belcher and Davis, 1971].

along the main field. The observed frequencies of the waves are from the order of minutes to hours. In Figure 3-12a the low power levels in the spectrum of $|B|$ compared to the spectrum of the variations of components is due to the dominance of Alfvén waves.

Observations also show fluctuations in the solar wind that are non-Alfvénic. For example, the leading edges of high velocity streams contain large amplitude Alfvén waves, a non-Alfvénic component, and also perhaps an Alfvénic component propagating toward the sun [Belcher and Davis, 1971]. These latter two types of waves are probably of local origin.

There are very few unambiguous identifications of interplanetary magnetoacoustic waves. One case reported by Burlaga [1968] is probably a fast magnetoacoustic wave propagating across the magnetic field [Barnes, 1979].

3.3. LARGE SCALE STRUCTURES AND DISCONTINUITIES

3.3.1 Discontinuities

Before discussing the types of disturbances that appear at 1 AU in the solar wind, it is helpful to describe the classifications of discontinuties more completely. For this purpose the hydromagnetic approximation is used, that is, the plasma flow will be approximated by the flow of a dissipationless perfect gas. The magnetic field will be assumed to follow the flow. The approximation will be sufficiently accurate to organize the observations of interplanetary disturbances and discontinuities discussed here. The quantities that must be conserved across a hydromagnetic discontinuity are mass, momentum, energy, the component of the magnetic field perpendicular to the discontinuity, and the component of the electric field tangential to the discontinuity. The jump conditions have been given by Spreiter and Alksne [1969].

For a tangential discontinuity:

$$v_n = H_n = 0 \tag{3.19}$$
$$[v_t] \neq 0, \ [H_t] \neq 0, \ [\rho] \neq 0, \ [P + H^2/8\pi] = 0,$$

for a contact discontiunity:

$$v_n = 0, \ H_n \neq 0, \ [v] = [H] = [P] = 0, \ [\rho] \neq 0, \tag{3.20}$$

for a rotational discontinuity:

$$v_n = \pm H_n/(4\pi\rho)^{1/2}, \qquad [v_t] = [H_t]/(4\pi\rho)^{1/2} \tag{3.21}$$
$$[\rho] = [P] = [v_n] = [v^2] = [H^2] = [H_n] = 0,$$

and fast and slow shock waves satisfy

$$v_n \neq 0, \; [\rho] > 0, \; [P] > 0, \; [H_n] = 0$$

$$\underset{\text{fast}}{(\rho v_n)} \geq \underset{\text{rot}}{(\rho v_n)} \geq \underset{\text{slow}}{(\rho v_n)} \tag{3.22}$$

$$H_t \text{ and } H^2 \begin{pmatrix} \text{increase} \\ \text{decrease} \end{pmatrix} \text{ through } \begin{pmatrix} \text{fast} \\ \text{slow} \end{pmatrix} \text{ shock waves.}$$

Here v, ρ, P, and H are the velocity, density, pressure, and magnetic field intensity respectively in a frame of reference at rest with the discontinuity. Subscripts t and n refer to components tangent to and normal to the discontinuity surface and [] denotes the difference in the enclosed quantity on the two sides of the discontinuity. The rotational discontinuity is the steepening of an Alfvén wave. Fast and slow shocks are the steepening of fast and slow magnetoaccoustic waves. Contact and tangential discontinuities do not propagate in a frame of reference at rest with the undisturbed plasma. The three other discontinuities do propagate in that frame. Contact discontinuities are not expected to be observed in the solar wind because they are difficult to form and would decay away quickly. Tangential and rotational discontinuities and fast and slow shocks have been observed. Slow shocks are very rare, and if not specifically stated otherwise, the word "shock" will be used here to refer to a fast shock.

At earth, three types of discontinuities are common, fast shocks and rotational and tangential discontinuities. Shocks are formed in the solar wind by the steeping of the interaction region between fast and slow solar wind parcels. They are commonly associated with impulsive high speed solar wind from flare events. The interaction region between long lived streams of slow and fast solar wind rarely steepens into shocks by the time the solar wind regions arrive at earth. Rotational and tangential discontinuities are commonly observed at 1 AU and are apparently formed close to the sun but the mechanism of formation is not known [Tsurutani and Smith, 1979]. Since the magnetic fields are measured in space with a smaller sampling interval than particles, most studies of discontinuities have used observational criteria based on changes in the magnetic fields. The frequency of occurrence of discontinuities will depend on the selection criterion but with carefully designed criteria it is found that tangential and rotational discontinuities occur at a rate of one or two per hour. The mean time interval between arrivals of discontinuities can typically be described by a Poisson distribution over the interval of from perhaps 10 minutes to an hour, but the rate of occurrence varies strongly on a time scale of several days. Even on a time scale of several solar rotations, the average rate varies by a factor of more than 2 [Tsurutani and Smith, 1979]. Two important parameters that characterize the discontinuities are the angle through which the magnetic field rotates and the percentage change

in the field magnitude. The distributions of these quantities are shown in Figure 3-15, adapted from Tsurutani and Smith [1979]. Small angle and magnitude changes occur most frequently. Discontinuities are usually quite abrupt. A study of Mariner 4 magnetic field data found that 50% of the discontinuities analyzed had thicknesses less than 3500 km and 10% less than 500 km [Siscoe et al., 1968].

A class of discontinuities called directional discontinuities (DD) has been defined as events that are either rotational or tangential discontinuities and show abrupt changes in magnetic field of at least 30° in consecutive 30-second magnetic field averages. It is not possible to unambiguously distinguish between tangential discontinuities and rotational discontinuities among DDs, but is was found that in low velocity solar wind tangential discontinuities are most common whereas DDs consistent with outward propagating rotational discontinuities become the predominant mode in high velocity winds [Solodyna et al., 1977].

Shock discontinuities are also observed at earth and are usually associated with solar events such as flares or perhaps errupting prominences. The fast solar wind from such an event accelerates the ambient wind in front of it. If the difference in velocity between the fast wind and the ambient wind is larger than the speed of a fast magnetohydrodynamic wave, a shock will form in the ambient wind at a position well in front of the boundary between the ambient wind and the flare plasma. This shock is known as the forward shock. As the fast plasma accelerates the ambient plasma, conservation of energy and momentum require the fast plasma itself to slow down. If the slowing down is severe enough another shock called the reverse shock will form within the fast plasma on the sun side of the boundary. When a detector passes through a forward shock, there will be a sudden increase in magnetic field, density, and temperature and a decrease in velocity. Passage through a reverse shock will appear as a decrease in magnetic field, density, and temperature and an increase in velocity. Both types of shocks have been observed as shown in Figure 3-16 [Burlaga and King, 1979]. Forward and reverse shocks are found in flare associated events and reverse shocks occasionally are formed during the interaction of long lived streams of slow and fast solar wind. However, shocks are not as common as DDs and occur once every few days at sunspot maximum and less frequently at low sunspot number.

The jump conditions at shocks (Rankine Hugoniot conditions) allow the strength of the shock and the direction of the normal to the shock to be determined if the plasma and field properties are known accurately enough. For strong shocks the direction of the normal to the shock can be found from

$$\mathbf{n} = \pm \, (\mathbf{B}_1 \times \mathbf{B}_2) \times (\mathbf{B}_2 - \mathbf{B}_1), \tag{3.23}$$

where $\mathbf{B}_1$ and $\mathbf{B}_2$ are the observed fields before and after shock passage and the sign depends on whether the shock is forward or reverse. A wide range of shock normals has
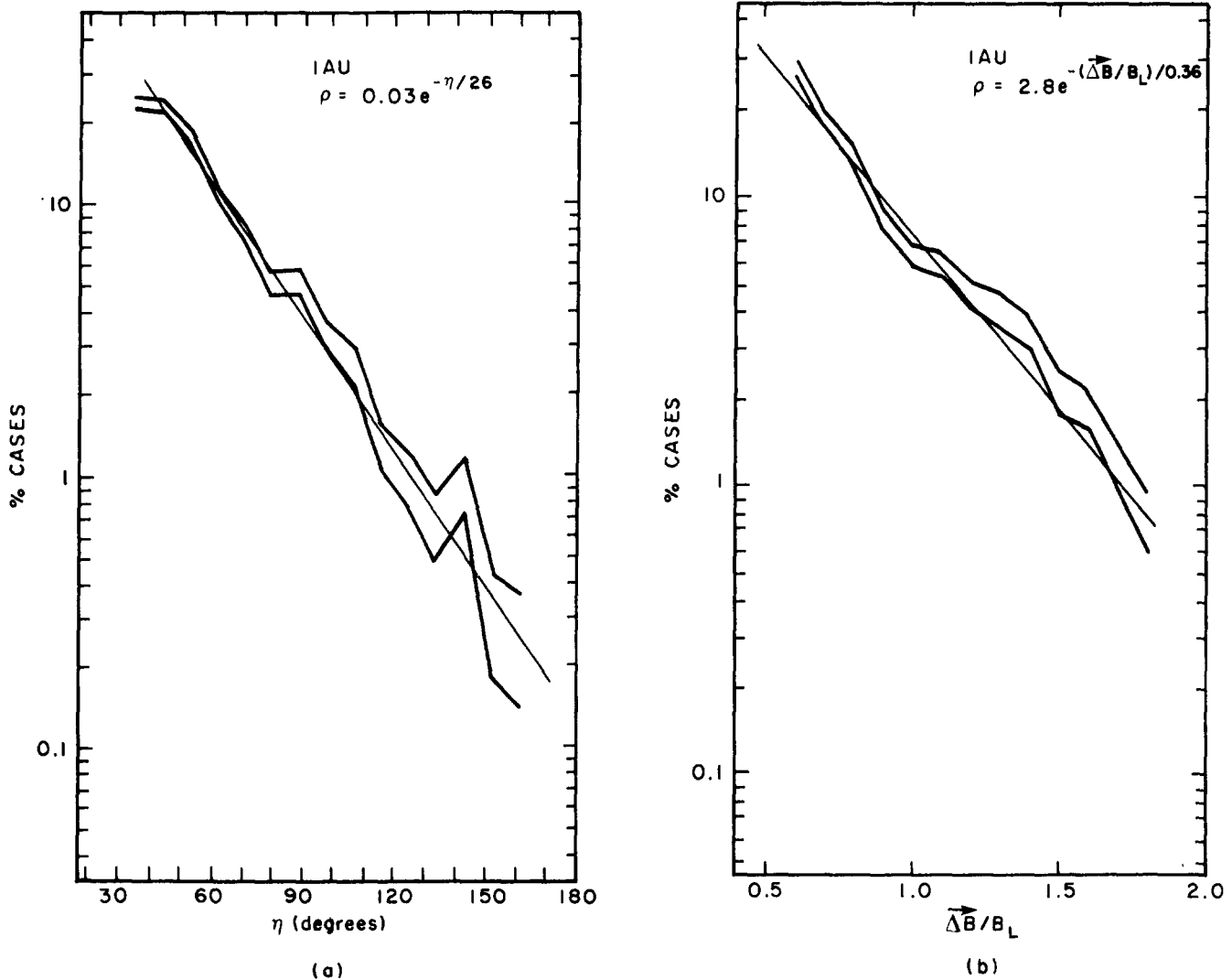
Figure 3-15. Normalized distributions of (a) the field rotation angle η across discontinuities and of (b) the relative field change $|\Delta B|/B_L$, where B_L is the larger of the field magnitudes on either side of the discontinuity. The two plots in each panel are the normalized distribution plus or minus one standard deviation [Tsurutani and Smith, 1979].

been observed, and although most normals lie within 45° or so of the earth-sun line, almost any orientation can occur. In addition, the flares that cause the strongest shocks tend to occur within 45° of the central meridian of the sun but sometimes flares occurring near the solar limbs cause shocks to appear at earth's orbit. The Mach numbers of most of the few shocks for which determinations have been made tend to be rather low, about 2 or 3, but stronger shocks do occur [Hundhausen, 1972].

3.3.2 Solar Wind Streams

The earliest continuous observations of the solar wind were those from Mariner 2 [Neugebauer and Snyder, 1966] which found that the solar wind speed and density were

variable, but both quantities also exhibited a good deal of order (Figure 3-17). During a 27-day rotation period of the sun, several intervals of higher than average speed occured. As seen in the figure, the high speed intervals tended to recur on the next rotation. The proton density typically maximized before the velocity. These high-speed corotating (that is, rotating with the sun) streams are one of the out-standing organized features of the solar wind. A particular stream may persist for many months or longer than a year. They are responsible for recurrent geomagnetic storms that characterize the declining phase of the sunspot cycle. The streams are imbedded within the sector structure, that is, magnetic sector boundaries typically precede the velocity rise by hours or days. The solar sources of the streams are the low temperature, open magnetic field regions known as coronal holes [Neupert and Pizzo, 1974].

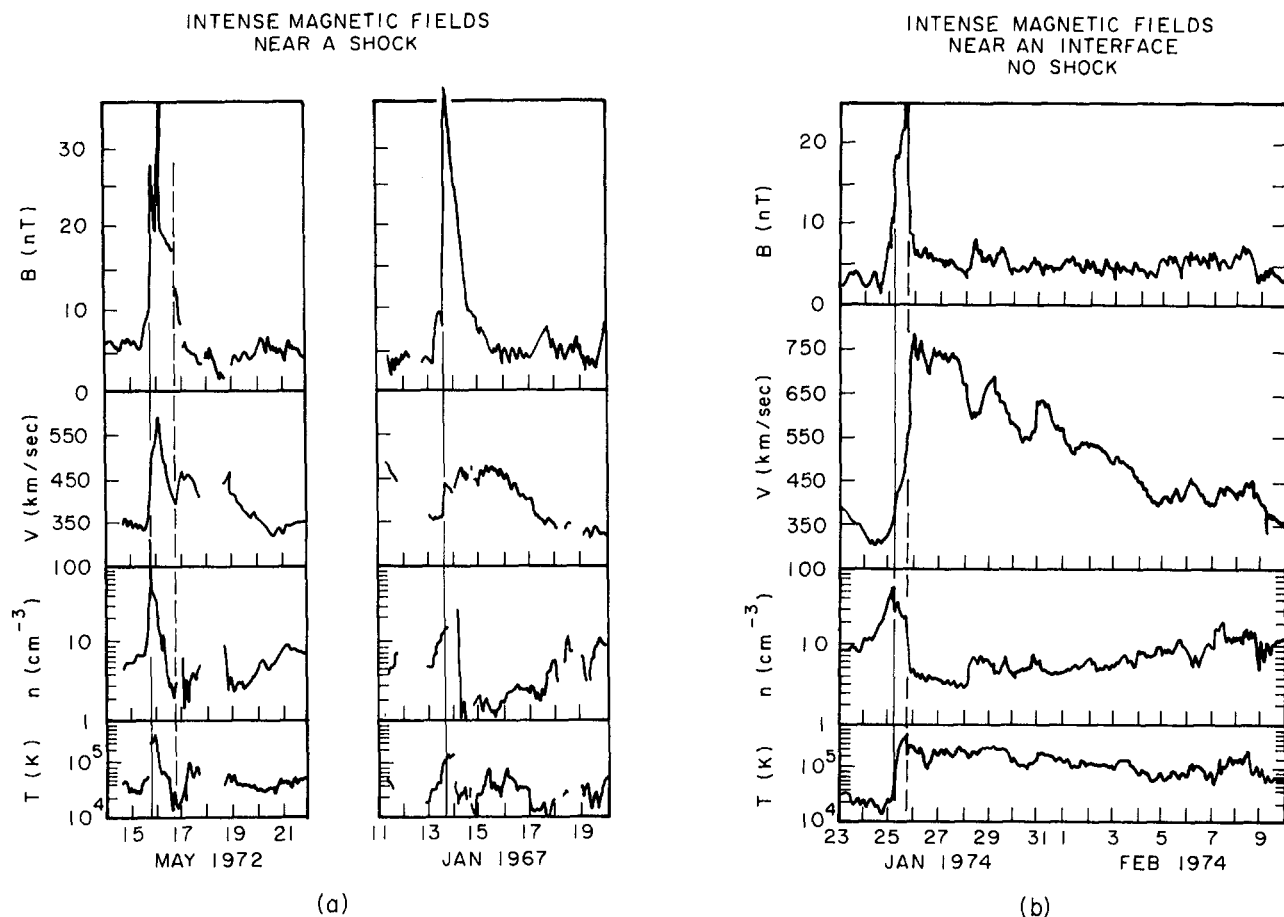The properties of the stream structure have been exten-

Figure 3-16. Shocks and stream interfaces. (a) gives hourly average data for two examples of shocks detected in the solar wind. Note the rise in velocity, temperature, density and magnetic field at the solid vertical line. The dashed line indicates the end of the shocked region. (b) shows a stream interface. The interface region is characterized by an abrupt drop in density and rise in temperature. It is the region between the density and temperature maxima and is bounded by the vertical lines. Although both the shocks and the interface region are characterized by very high magnetic fields in these examples, that feature does not always occur (see Figure 3-23 for magnetic field behavior across a shock), [Burlaga and King, 1979].

sively analyzed. The structure observed at 1 AU is partly due to the structure of the wind as it leaves the sun, and partly to the evolution of that structure due to the interaction of low and high speed streams emmitted from a rotating sun. An intuitive idea of the interaction is easily developed by the following picture. Assume low speed wind leaves the sun's neighborhood to the west of the source of high speed wind, that is, at a position further along in the direction of rotation. This means that as the sun rotates the high speed region rotates to the angular position previously occupied by the low speed source region. Then, viewed along a radius vector to the sun, the low speed parcel of wind will have a high speed parcel of wind overtaking and compressing it. As the high speed material increases the velocity of the low speed material, the low speed material will become compressed. At the same time, due to conservation of momentum, the high speed material will be slowed and its density will increase. Thus a ridge of high density

material will form on both sides of the boundary between the streams.

The boundary between low and high speed streams has a distinctive character and is called a stream interface region. It is characterized by an abrupt drop in density, a sharp rise in temperature, and a rise in velocity that may be small. An example of a stream interface is given in Figure 3-16 [Burlaga and King, 1979]. This figure also shows an example of an interface associated with a very intense magnetic field. Magnetic field change is not a defining characteristic of interfaces and often is not present.

A study of the characteristics of selected solar wind streams was made by Gosling et al. [1978] who superposed data using 23 very abrupt interfaces as the zero time point for the data. The data were extremely well ordered by this procedure, as is seen in Figure 3-18. The figure gives the one hour average data for 100 hours both before and after the interfaces. The error bars are the estimated error of the
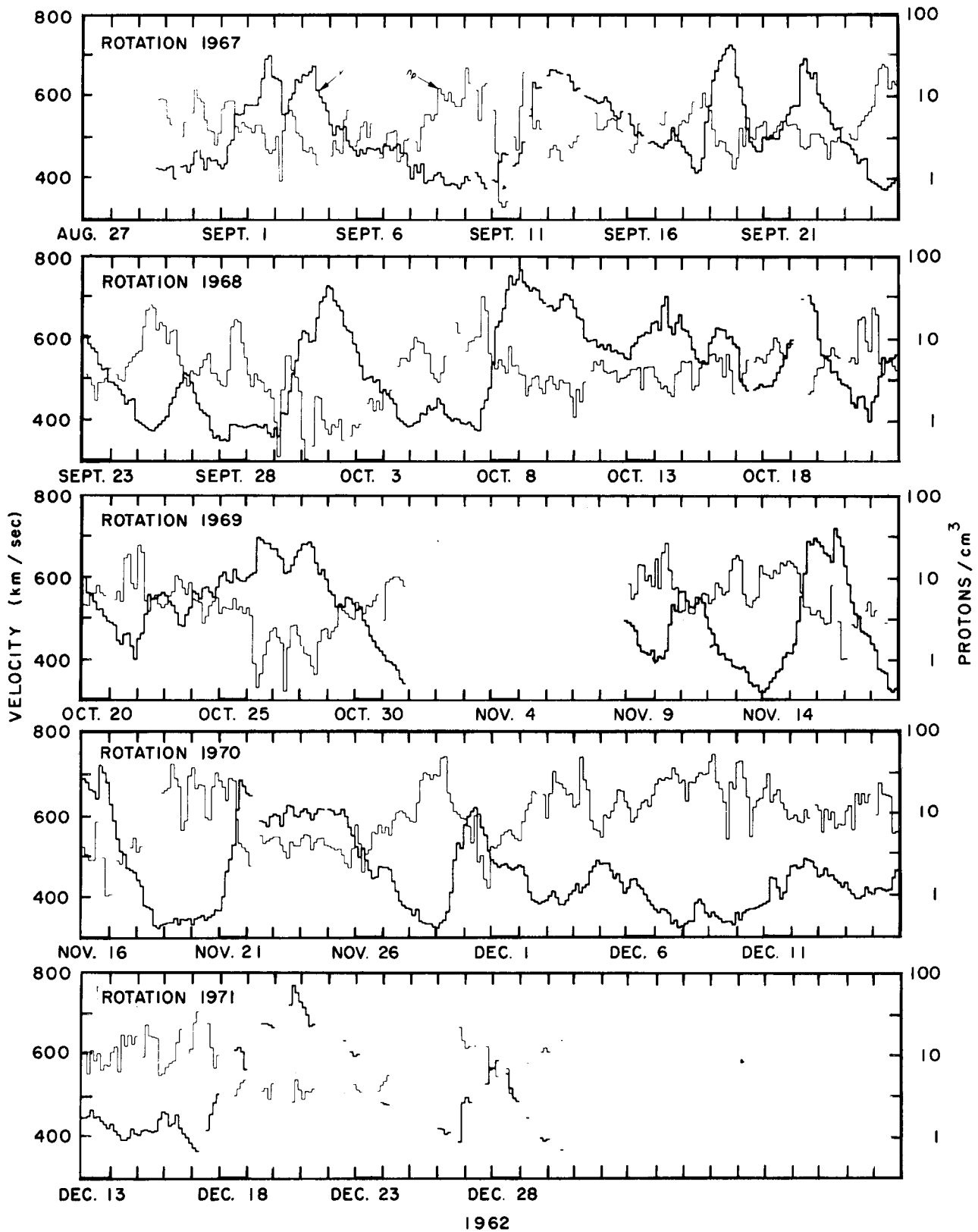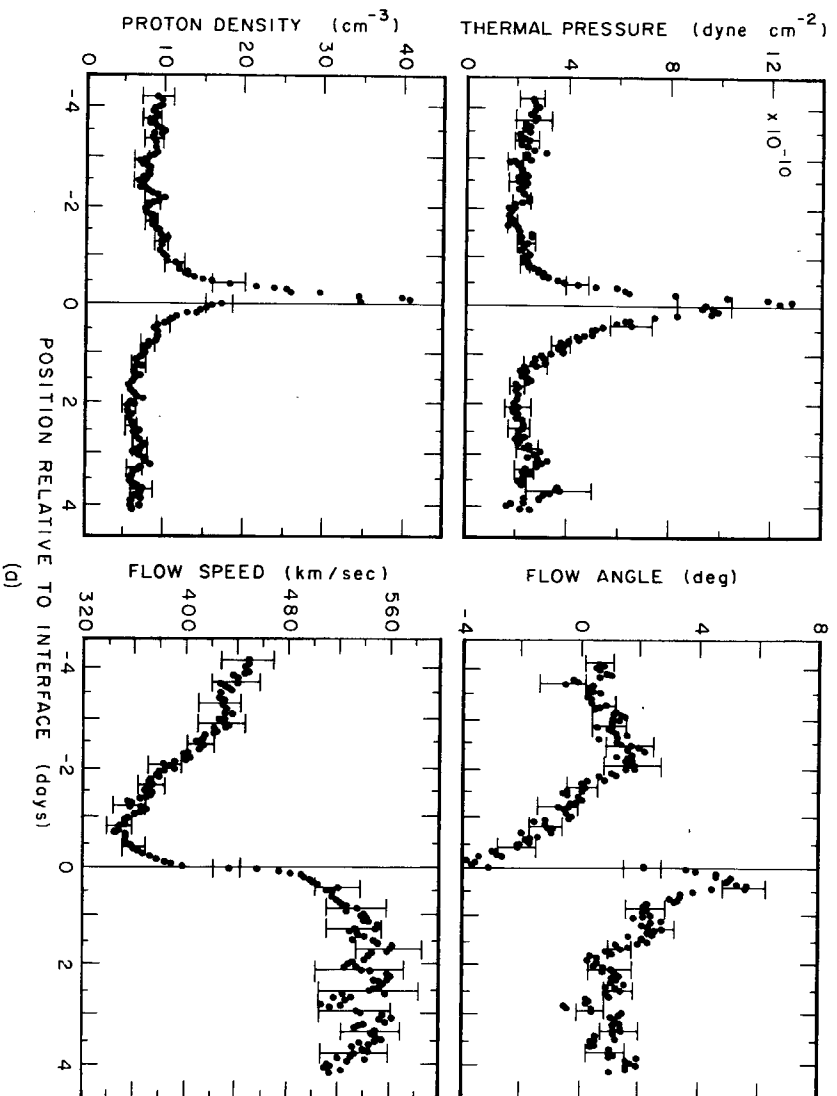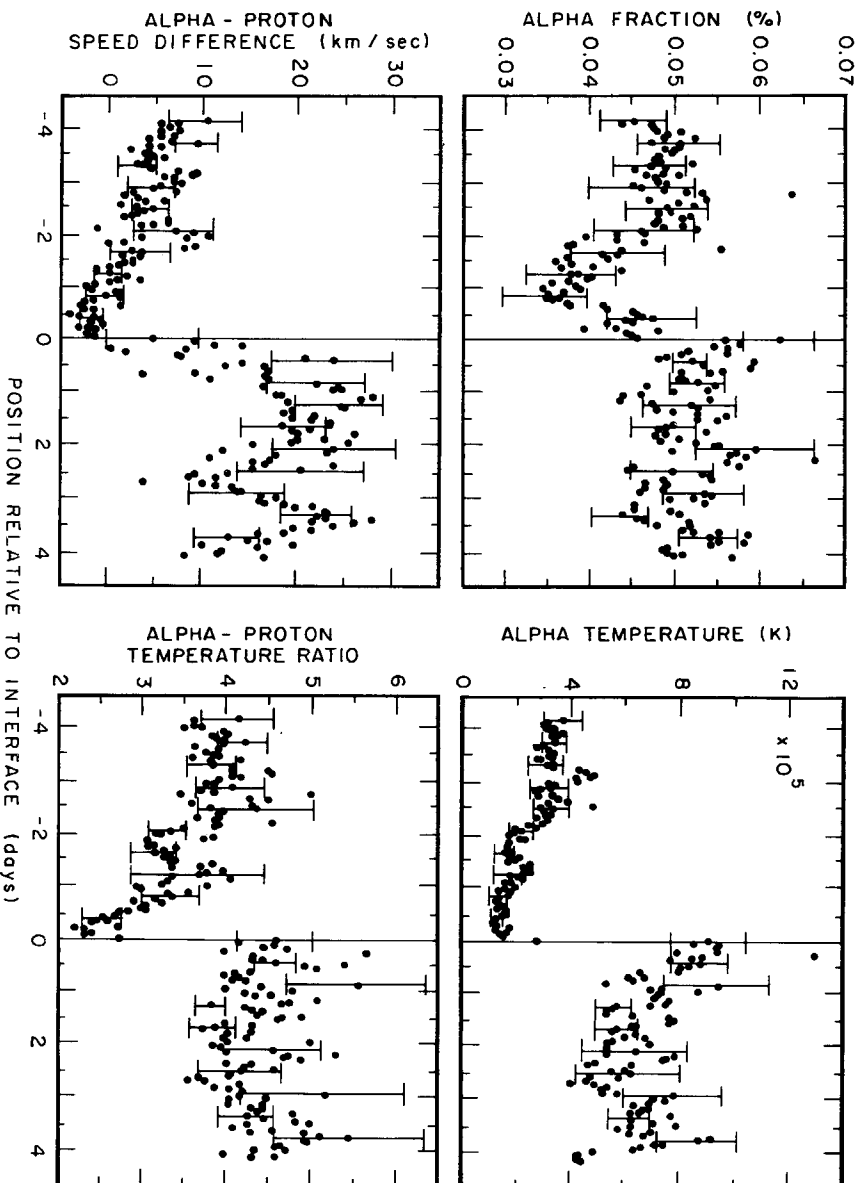
Figure 3-17. Three-hour averages of the solar wind proton density (light line) and flow speed (heavy line) from Mariner 2 on its flight toward Venus in 1962. Each panel presents 27 days of data. Note the velocity stream structure and the tendency for recurrence of streams on each solar rotation [Neugebauer and Snyder, 1966].
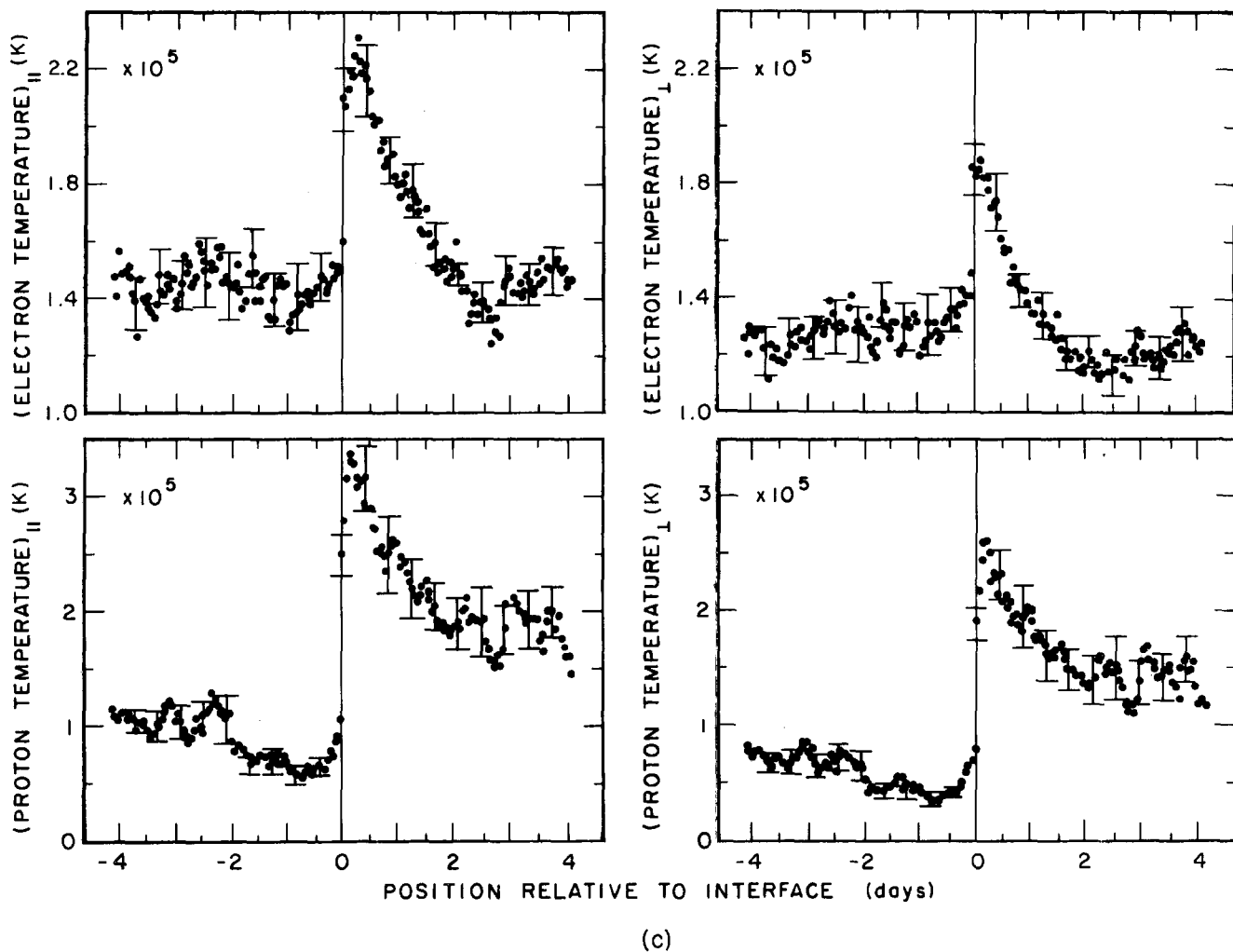
(a)

(b)

Figure 3-18. Superposed epoch analysis of one-hour average plasma properties in 23 streams. The zero time is defined as being the time of an abrupt interface. No streams with more gradual interfaces (Figure 3-16) were included in the analysis [Gosling et al., 1978].

mean. Figure 3-18a gives the proton thermal pressure, the proton density, the flow angle in the ecliptic plane and the flow speed. The interface occurs when the speed is still quite low, about 400 km/s. Three hours after interface passage, the average speed is about 480 km/s, but the maximum average speed of 560 km/s is not reached until 1.5 days later. The plasma near the interface is accelerated by the stream-stream interaction. Since the interaction region has the shape of an Archimedes spiral (for the same reasons discussed in Section 3.2.2, for the magnetic field direction) the low speed plasma is deflected toward the west whereas the high speed plasma is deflected towards the east. A shear flow occurs at the interface. Magnetic sector boundaries occur in the low speed wind preceding the interfaces. They typically appear from 1.5 days to 1.5 hours before the interfaces. The total pressure (that is, particle plus magnetic field) peaks approximately at the interface although the proton density and proton thermal pressure are already declining at that position. On the average there is discontinuity in

density of about 7 cm^{-3} at the interface. This discontinuity takes place on a time scale of minutes.

Figure 3-18b gives the temperatures of the protons and electrons parallel and perpendicular to the magnetic field. All four quantities change discontinuously at the interface and both electron temperatures return to near their low speed values three hours after the interface passes, but both proton temperatures remain elevated. Note that the temperature scales are not the same for the protons and electrons and that the electron temperature increase is relatively small.

The properties of the helium in the solar wind also show organization when analyzed according to stream structure. Figure 3-18c shows that the abundance of helium minimizes about a day before the interface and that both the helium temperature and the ratio of alpha particle temperature to proton temperature are discontinuous. In most of the stream structure the helium is, on average, flowing faster than the hydrogen, but during the day before the interface is crossed the relative velocity changes sign, and in this region, the

3-21

CHAPTER 3

proton speed exceeds the alpha particle speed by a few km/s.

3.3.3 Solar Flare Disturbances

The second major interplanetary structure that orders the solar wind is the solar flare disturbance. Major flares eject high speed plasma into the wind, which results in a disturbance propagating to the earth and beyond. The disturbance is shown schematically in Figure 3-19 [Bame et al.,
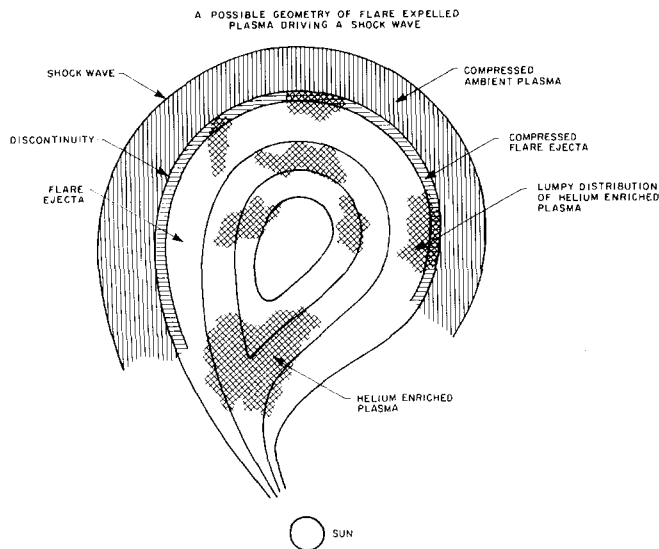

Figure 3-19. A schematic diagram of a possible geometry for the solar wind disturbance caused by a major solar flare [Bame et al., 1979].

1979]. The rapidly moving flare plasma compresses the ambient wind before it and a shock is formed. Studies indicate that for major disturbances the shock expands on a broad front so that its shape when the shock arrives at 1 AU can be approximated by a half circle of radius 0.6 AU and center 0.4 AU [Hirshberg, 1968; Rickett, 1975]. At the shock the density, proton temperature, magnetic field, and velocity increase abruptly as the shocked gas is entered. The density and velocity may or may not continue to increase in the post shock region depending on the details of the delivery of energy from the flare site to the solar wind and also on the structures through which the shock propagated on its way from the sun to the earth. For example, if a shock is observed in the low speed wind preceeding or following a stream, the density and velocity change at the shock will be relatively large. However, if observed near the density peak or in the high speed wind, a disturbance with the same initial conditions at the sun will show a relatively small change in velocity, although the change in density may still be considerable [Hirshberg et al., 1974]. A discontinuity between the shocked ambient plasma and

the driven gas is shown in Figure 3-19, but its exact position is often very difficult to identify observationally. A reverse shock may form behind the discontinuity.

The driver gas itself, which typically arrives at earth about 5–10 hours after the shock, is often characterized by enhancement in the helium abundance that commonly exceeds 15% helium by number and may reach more than 20%–25% [Hirshberg et al., 1972]. On some occasions the helium enhancement is not seen or it may be seen later in the event. In Figure 3-19 this is interpreted as indicating a patchy distribution of helium enhanced plasma. The number of particles released into interplanetary space by major flare events is estimated to be on the order of 10^{39}–10^{40} particles or 10^{15}–10^{16} g. The driver gas is often also characterized by low proton [Gosling et al., 1973] and/or electron temperatures and bidirectional streaming of electrons. These observations suggest that the magnetic field can form closed loops as shown in Figure 3-19. Such loops have apparently been observed [Burlaga et al., 1981]. Examinations of the ionization states of heavy ions in plasma associated with flares indicate that at least part of the flare ejecta originates in coronal regions with temperatures of 3–4 $\times$ 10^6 K. The driver gas has been slowed down on its way from the sun to the earth by interaction with the ambient solar wind. Thus the observed velocity of the driven gas will be less than the mean transit velocity of that gas from the sun to the earth. Typical values of the ratio of observed velocities to mean transit velocities for a series of major flare-shock events is about 0.8 [Hirshberg et al., 1972]. The interplanetary magnetic field during flare disturbances often reaches very high values (30–40 nT) in the direction perpendicular to the ecliptic plane. Since the velocity of the driver and disturbed gas is high, and if these strong fields are southward, then the solar wind will interact strongly with the earth's magnetic field and will drive impressive geomagnetic storms and auroras. The storms reflect the structure of the flare disturbance. The classical storm begins with a sudden commencement caused by the abrupt increase in dynamic pressure on the magnetopause that occurs when the shock is crossed. The initial phase of the storm, during which the earth's field is enhanced but not disturbed is due to the shocked region flow when the magnetic field in that region is northward. When and if the field turns southward the main phase of the storm develops.

3.4 LONG TERM VARIATIONS

3.4.1 Solar Cycle

It was expected that the interplanetary medium varied with the solar cycle even before in situ observations of the solar wind began. Fluxes of particles from the sun were believed to be the cause of geomagnetic activity and aurora and it was well established that these phenomena exhibited

a solar cycle variation. The variation of the solar output during the eleven year solar cycle has many manifestations; for example, sunspot numbers, major solar flares, and the solar wind velocity. Distinctions should be made between the solar cycle as expressed in each of the various quantities. Although all solar cycle variations will have the same period they may have different phases, relative amplitudes, and shapes. It is common practice to use the variations of sunspot numbers as the standard for the solar cycle and to compare the changes in all other quantities to the sunspots. Here the term "solar wind cycle" will be used to denote the changes in the various interplanetary parameters.

Before direct observations were begun, studies of geomagnetic activity had shown that the variations in the interplanetary medium were such that minimum solar cycle conditions at earth's orbit occurred (on the average) about 1 to 1.5 years after sunspot minimum. Also, geomagnetic storms characterized by sudden beginnings were most common at sunspot maximum, but storms tending to recur on successive solar rotations were more common about three years after maximum. The sudden commencements are due to solar wind shocks which are most common at sunspot maximum. Recurrent storms are caused by long-lived relatively steady high speed streams in the solar wind such as those observed in 1962 and 1973–74, that is, during the phase of decreasing sunspot numbers.

The solar wind has now been observed at least intermittently for almost 20 years and solar cycle variations of several parameters have been established. Figure 3-20 [Feynman, 1983] shows the variations of some of these quantities. Figure 3-20a gives the annual mean sunspot number from 1962 to 1978. Figure 3-20b shows the annual mean velocity of the solar wind. The first few values are joined by a dashed line to indicate that the data sample was too small to give an accurate value.

There is also a solar cycle variation in the magnitude of the interplanetary field that is most clearly seen in the yearly mean value of the logarithm of $|B|$ as shown in Figure 3-20c. The data exhibit relatively low mean values, corresponding to $|B|$ about 5 nT in 1964, 1965, 1975, 1976 and 1977. The mean log $|B|$ is remarkably constant throughout the cycle between 1966 and 1974 corresponding to $|B|$ about 5.8 nT. The large rise to $|B|$ about 6.9 nT appearing at the beginning of the new sunspot cycle shows that the solar wind magnetic field can differ from cycle to cycle.

The yearly averages of the hourly averaged magnitude of $B_z, \langle |B_z| \rangle$, are also compared to the sunspot number in Figure 3-20d. Here B_z is defined in GSE coordinates and the hourly average is taken by including the sign of B_z, that is, if B_z were of constant magnitude and negative for half of the hour and positive for the rest, $|B_z|$ would be zero. There are two maxima in $\langle |B_z| \rangle$, one before and one after sunspot maximum. It is not known if this double maximum is a common form of the $\langle |B_z| \rangle$ solar cycle variation.

The variation in the yearly average solar wind speed $\langle v \rangle$ from 1966 to 1978 is shown in Figure 3-20b. Data before
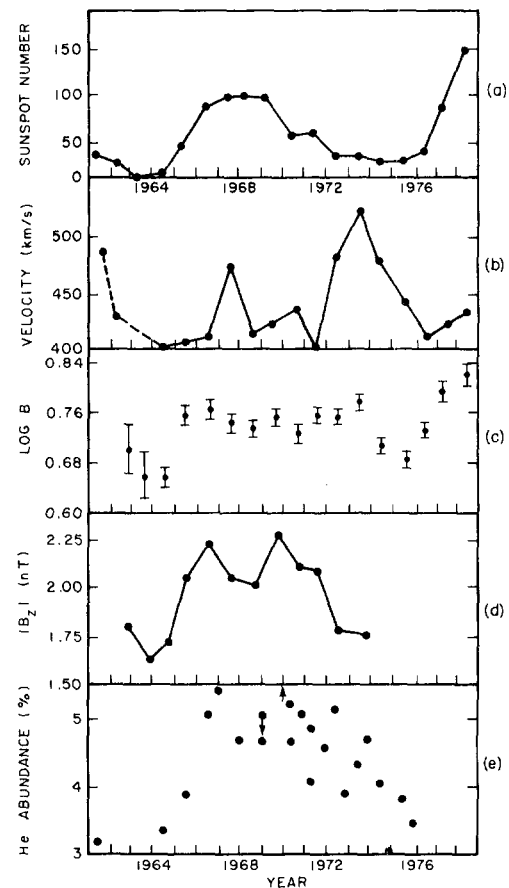

Figure 3-20. Long term variations of selected quantities. The top panel (a) shows the annual mean sunspot number. The second panel (b) gives the annual mean velocity. The third panel (c) shows the yearly averaged values of logarithms of hourly interplanetary magnetic field magnitudes. The observed distribution of hourly IMF is log normal. The fourth panel (d) shows the yearly average of hourly values of the magnitude of the z component of the IMF. The final (e) panel gives the percentage abundance of helium by number. The arrows indicate that only limits on the values could be determined [Feynman, 1983].

1966 were sparse but what information there is indicates that the mean velocity observed in 1962, during the declining leg of solar cycle 19, was high with a velocity of about 490 km/s whereas in 1964 and 1965 it was near 400 km/s. The distinction between the shape of the sunspot cycle variation and the solar wind cycle variation is clearly shown by the velocity. Here the highest yearly average velocities are observed during years dominated by recurring high speed solar wind streams. That this is nonetheless a solar cycle variation is shown by the fact that the declining phase of each sunspot number cycle exhibits such a series of recurrent geomagnetic storms.

The averaged helium abundance in Figure 3-20e shows a solar cycle variation much more like that of the sunspot number. The abundance near sunspot minimum in 1962–65 and 1976 is just above 3%, whereas 5% was the abundance typical of sunspot maximum conditions.

CHAPTER 3

3.4.2 Secular Variations

Little information exists on the variation of the solar wind for time scales longer than a solar cycle. In Figure 3-20c it appears that the interplanetary magnetic field intensity in 1979 near the maximum of the current solar cycle was larger than at any time in the past, but Figure 3-20b shows that the velocity was quite close to values typical of the preceding maximum. It has also been inferred from geomagnetic records that the solar wind was in some sense weaker during the early years of this century than it has been recently [Feynman and Crooker, 1978], and from auroral records that it was also weak in the early years of the 19th century [Feynman and Silverman, 1980]. The lack of aurora during the Maunder minimum in the 17th century again indicates a weak wind [Suess, 1979]. A revaluation of the auroral record from 450 AD to 1450 AD convincingly shows a periodicity in occurrence frequency with an average period of about 87 years [Siscoe, 1980] which almost certainly reflects a solar wind variation.

3.5 THE CLOSE NEIGHBORHOOD OF THE EARTH

3.5.1 Magnetosheath

As the magnetized solar wind flows past the earth, the plasma interacts with the earth's magnetic field and confines the field to a cavity, the magnetosphere. Since the proton flow of the solar wind is almost always highly supersonic and super-Alfvénic, a shock, called the bow shock, forms sunward of the magnetospheric cavity. The configuration is shown schematically in Figure 5 of Chapter 8. The solar wind flows across the bow shock in front of the earth where it is slowed to subsonic velocities. It is deflected by the obstacle presented by the earth's field at the boundary designated as the magnetopause in Figure 8-5. The wind then flows generally antisunward down the flanks of the magnetosphere carrying the interplanetary field with it. A typical distance between the earth's center and the subsolar point on the magnetopause (the boundary between the solar wind and the magnetosphere) is 10 earth radii (R_E). The shock is about 3 R_E sunward of the magnetopause at the subsolar point. The region between the shock surface and the surface of the magnetosphere is called the magnetosheath.

The problem of calculating the flow of the solar wind plasma past the earth using the full plasma equations is prohibitively difficult. Even in the magnetohydrodynamic approximation, the problem has not been treated in general. The high conductivity of the solar wind and the large kinetic energy density of the particles permits the approximation to be made that the magnetic field configuration can be treated as though the field is frozen into the flow. Although the solar wind proton mean free path for Coulomb collision is

typically 1 AU at earth's orbit, the plasma acts as a fluid on a much smaller spatial scale, because plasma instabilities and wave particle interactions produce a small equivalent mean free path. For many applications it is good approximation to treat the solar wind as a magnetohydrodynamic fluid interacting with the earth's field. For a full discussion of the interaction of the wind and the magnetosphere the process of magnetic reconnection or merging is important; however, its major effect is to feed energy into the magnetosphere rather than to affect the flow around the magnetosphere and so it is beyond the scope of this chapter. See Chapter 8. A further simplification is usually made in the calculations by assuming the Alfvén Mach number of the solar wind flow is large. This decouples the fluid equations from the magnetic equations so that the properties of the flow can be determined by solving the gas dynamic equations, and subsequently the magnetic field can be found from the flow.

The shape of the forward part of the magnetosphere is calculated by neglecting the magnetic field pressure in the solar wind outside the magnetosphere boundary and the particle pressure inside the boundary. The remaining pressures are then set equal on the two sides, that is, the dynamic pressure of the solar wind flow outside is balanced by the magnetic field pressure inside.

The flow around the magnetosphere can then be calculated. To simplify the calculations further the magnetosphere is often approximated as an axisymmetric body formed by the rotation of the equatorial trace of the magnetosphere boundary around the earth sun line. The resultant flow is quite sensitive to the ratio of specific heats γ. Observations favor a γ of 5/3 [Auer, 1974] and this value was used in the model calculations discussed here.

The model flow in the high Mach number approximation is illustrated by Figure 3-21 [Spreiter and Alksne, 1969]. In Figure 3-21a, the lines of constant ratio of magnetosheath density to solar wind density are shown. The sheath density is high in the forward part of the magnetosphere reaching a maximum in the subsolar region. As the plasma flows back toward the magnetospheric flanks, it becomes less dense and values less than one begin to appear near the magnetopause at about 7 R_E behind the earth. Figure 3-21b shows both lines of equal velocity ratio and temperature ratio. Since the fluid approximation is used, the temperatures of the electrons and protons are assumed to be the same, and for comparison with observation they are assumed equal to the measured proton temperatures. The numbers labeling the lines and written on the magnetopause side of the magnetosheath are the temperature ratios, and the numbers on the bow shock side are the velocity ratios. The stagnation point is labeled at zero velocity, which of course is unrealistic as far as expectations of observations are concerned. However, slowing and heating of the plasma in the subsolar stagnation region is observed. As the plasma moves back along the flanks it begins to cool and increase in speed. Figure 3-21c shows the stream lines of the flow.
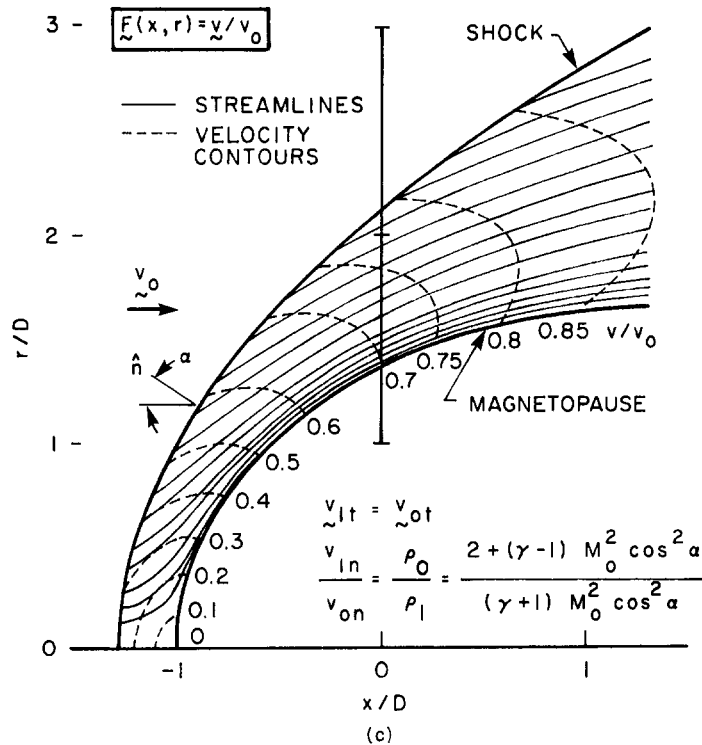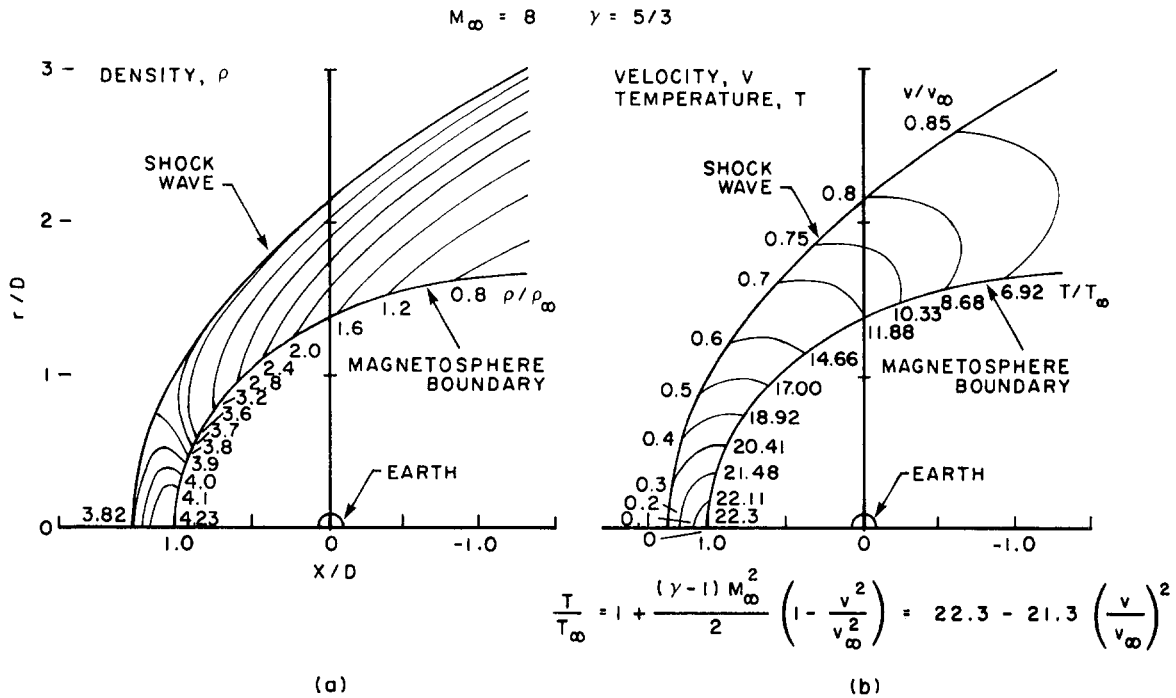
$M_\infty = 8 \qquad \gamma = 5/3$

$$\frac{T}{T_\infty} = 1 + \frac{(\gamma - 1) M_\infty^2}{2} \left(1 - \frac{v^2}{v_\infty^2}\right) = 22.3 - 21.3 \left(\frac{v}{v_\infty}\right)^2$$

(a)   (b)

$$\underset{\sim}{v}_{lt} = \underset{\sim}{v}_{ot}$$

$$\frac{v_{ln}}{v_{on}} = \frac{\rho_0}{\rho_1} = \frac{2 + (\gamma - 1) M_o^2 \cos^2 \alpha}{(\gamma + 1) M_o^2 \cos^2 \alpha}$$

(c)

Figure 3-21. Flow in the magnetosheath in the gas dynamic approximation for the high Mach number case (M = 8). (a) gives the density and (b) the temperature and velocity contours. The subscript ∞ denotes quantities in the undisturbed wind at "infinity". The non-subscripted quantities are the parameters within the magnetosheath. Lines of constant ratio of magnetosheath in undisturbed quantities are given. The shape of the contours for velocity and temperature are the same but the ratios differ as marked. The jump relation for the temperature is given in (b). In (c) the velocity contours are given again, along with the stream lines. The formula at the bottom of (c) gives the jump relations across a shock of arbitrary angle with the incident flow. Subscript 1 indicates values just behind the shock. The abscissas are normalized so the distance from the center of the earth to the subsolar point on the magnetopause is taken as one [Spreiter and Alksne, 1969; Spreiter et al., 1966].
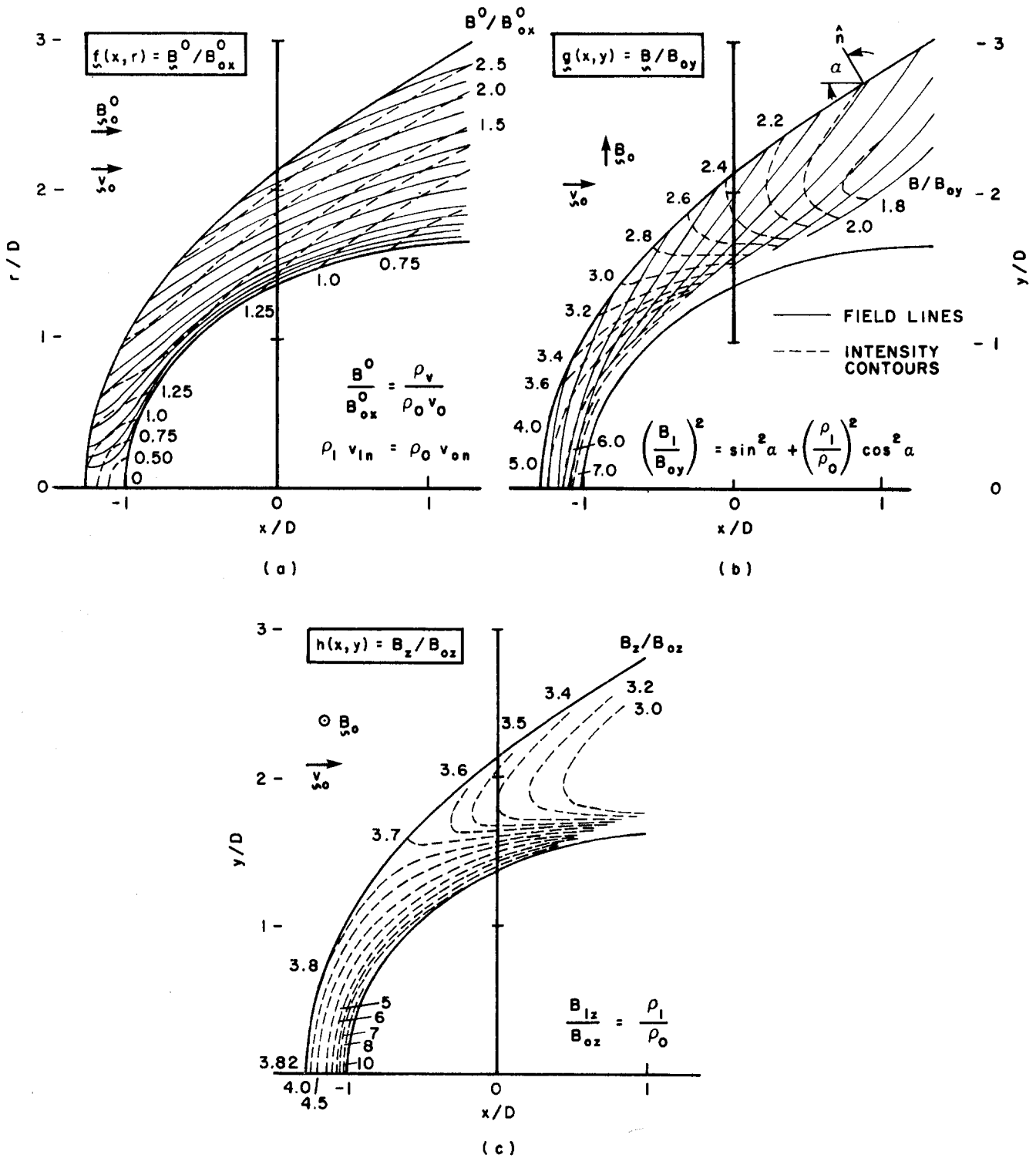
Figure 3-22. Magnetosheath magnetic fields for three orthogonal components of the interplanetary field calculated by assuming the field is frozen into the flow shown in Figure 3-21. The field directions are as shown in (a), (b), and (c). The jump relations at the shock are indicated and the dashed lines indicate contours of equal intensity ratio, whereas the solid lines follow the directions of the field lines [Alksne and Webster, 1970]. (Reprinted with permission from Pergamon Press, Ltd. © 1970.)

The magnetic field configuration is computed in this approximation by assuming the field is carried by the flow. The results are shown in Figure 3-22 [Alksne and Webster, 1970]. The incident field has been broken up into three orthogonal components with directions as shown on the figure. An arbitrary incident magnetic field will be described by an appropriate superposition of the three cases. The stream lines are given by the solid lines and the lines of equal magnetic field ratio are given by the dashed lines. The magnetic field lines become draped over the magnetosphere and tend to be aligned with the magnetopause direction.

Calculated values of magnetosheath electric fields are shown in Figure 3-23 [Alksne and Webster, 1970] but these have not been measured. Since there is no electric field associated with field aligned flow, electric fields for only two orthogonal magnetic field directions are shown, and the electric field due to an arbitrary magnetic field can be found by combining the two cases shown.

Measurements of the shape of the magnetosphere show some asymmetry that is not present in the results calculated from the high Mach number approximation. This asymmetry probably arises because of the the asymmetric magnetic field in the magnetosheath and the coupling between the fluid flow and the magnetic field. All of these effects will lead to magnetosheath pressure asymmetries which will distort the magnetosphere to some extent. In addition, the orientation of the earth's magnetic dipole relative to the direction of incidence of the solar wind must be taken into account.

The observed flow and averages of the magnetic fields in the magnetosheath agree satisfactorily with the magnetohydrodynamic models. The magnetosheath magnetic field is typically very disturbed but the vectors tend to be aligned with the magnetopause as shown in Figure 3-24a [Fairfield, 1967]. The average relative magnitudes of the magnetosheath field for 10 R_E intervals along the earth-sun line are shown in Figure 3-24b [Behannon and Fairfield, 1969]. The ratio of the magnitude of the magnetosheath field to the magnitude of the interplanetary field varies from 4 near the most sunward portion of the bow shock to less than 1 far down the flanks.

The variability of the magnetosheath fields is reflected in the power spectra as shown in Figure 3-25 [Fairfield, 1976]. The low frequency power levels of the variations of the field magnitudes differ by four orders of magnitude depending on the day. The September and November 1967 spectra are probably the most representative. Spectral peaks near 0.05 Hz and 0.07 Hz are typical but the exact frequency and relative magnitude are variable. The 31 July spectrum was taken on a day when the solar wind Mach number was low. At these times the power in magnetosheath variations is also quite low. The dashed lines with slopes of $1/f$ and $1/f^3$ are shown for comparison. The spectra typically steepen at frequencies above the proton gyrofrequency. At frequencies between 3.3×10^{-4} and 2.6×10^{-3} Hz, which are lower than those shown in the figure, the average slope is slightly steeper than $1/f$. There is a tendency for the per-
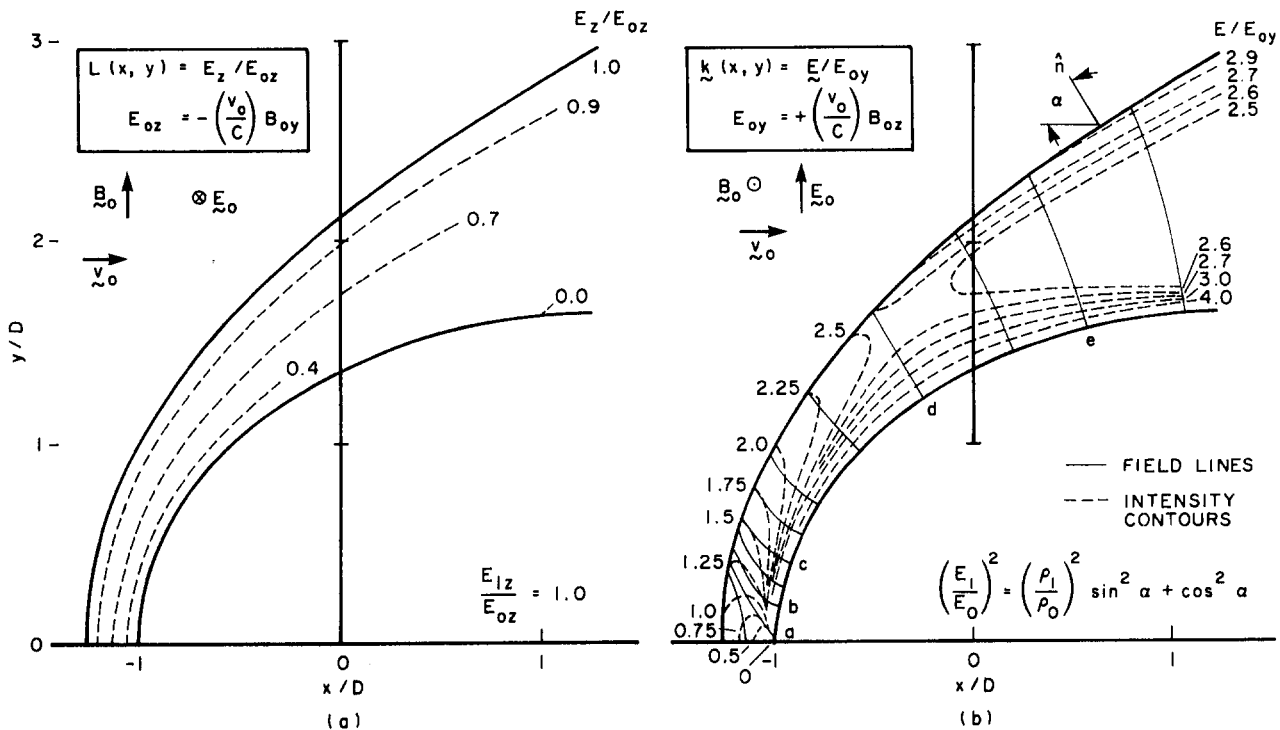

Figure 3-23.   Magnetosheath electric fields calculated under the same assumptions as in Figure 3-22. The relations at the shock jump are indicated in each panel [Alksne and Webster, 1970]. (Reprinted with permission from Pergamon Press, Ltd. © 1970.)
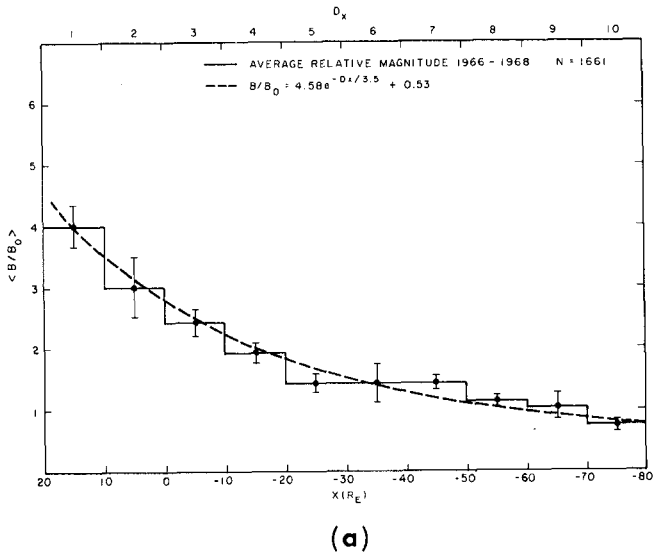
(a)

Figure 3-24. Observations of the magnetosheath field: a) Averages of the magnetosheath magnetic field intensity normalized to the simultaneously measured interplanetary field. For each ΔX bin measurements are taken from all available values of y and z. The field is intense in the subsolar region and decreases to less than the interplanetary value in the distant flanks [Behannon and Fairfield, 1969]. (Reprinted with permission of Pergamon Press, Ltd. © 1969.) b) Projections of vectors measured in the magnetosheath into the X, y plane for four different orientations of the interplanetary field, [Fairfield, 1967].
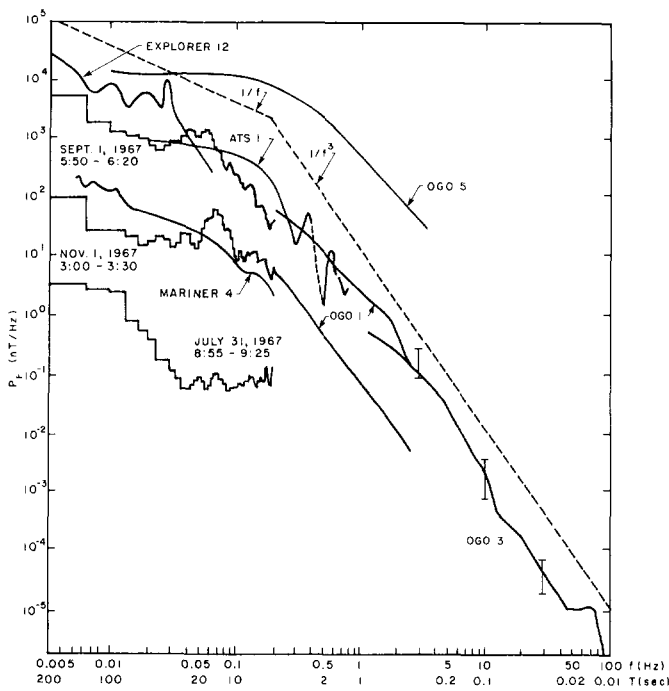

(b)
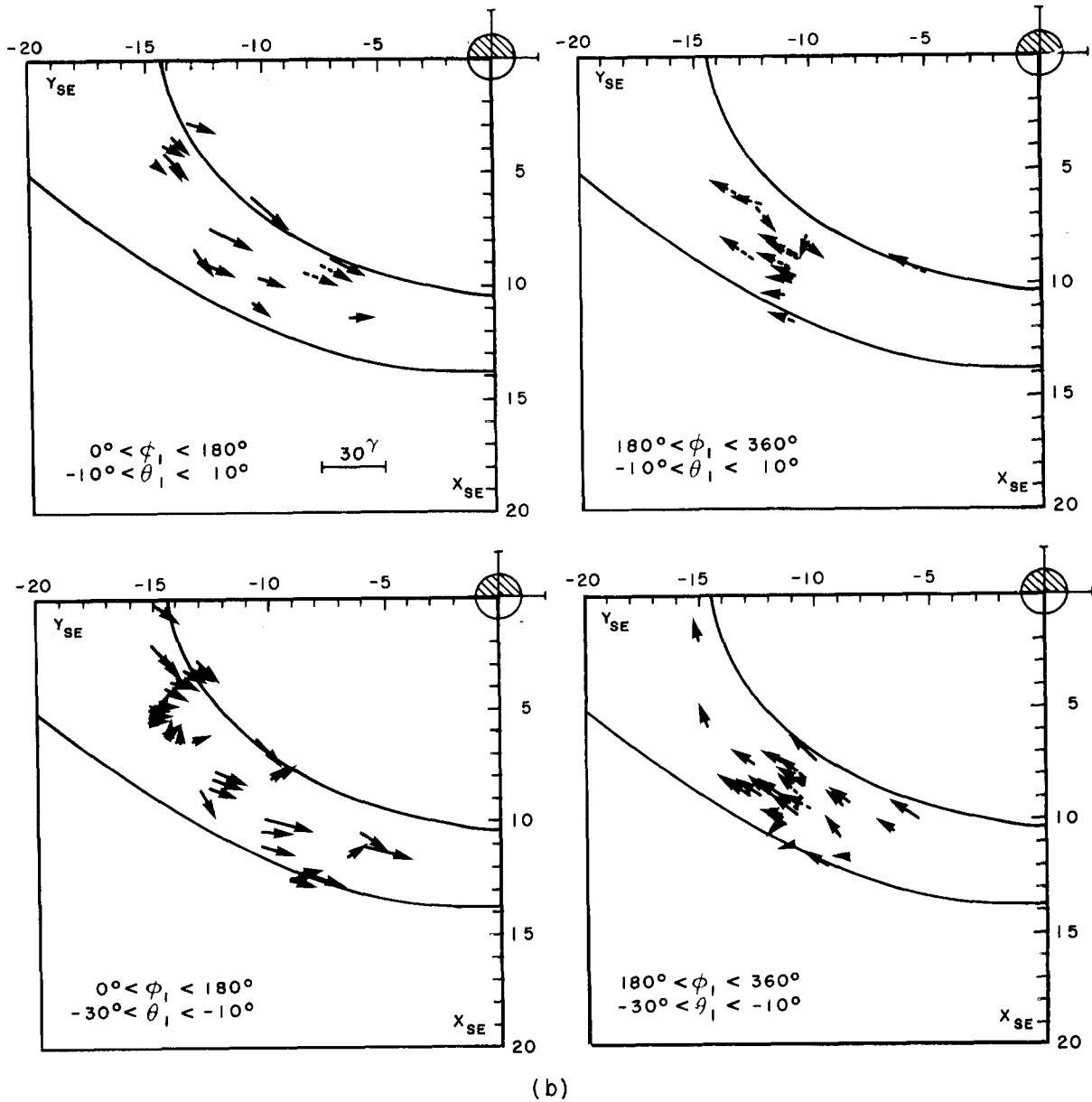
Figure 3-25. Composite of magnetosheath magnetic field spectra. The lower frequency data are magnetic field magnitude spectra while the highest frequency data are from fluctuations in the field components [Fairfield, 1976].

turbation vector to align itself with the shock surface for variations observed near the shock surface. In the inner portion of the magnetosheath, large amplitude waves occurring primarily in the field magnitude are observed. Rotational wave modes have been found to dominate over magnetoacoustic modes for wave periods greater than 10 minutes. There also appear to be plasma clouds with scales of several hundred to several thousand kilometers associated with weak fields that deviate from a direction tangent to the magnetopause. In addition to broad noise with a $1/f^3$ spectral shape there are often sporadic occurences of quasi-monochromatic bursts throughout the magnetosheath. These waves have a frequency of 50–200 Hz, durations of less than one to tens of seconds and amplitudes of tenths of nanoteslas.

Several sources have been suggested for magnetosheath field fluctuations. The waves and discontinuities in the solar wind are sources of some of the variability, as is the convection into the magnetosheath of waves produced at the bow shock or in the region of space just upstream from the bow shock. Waves incident on the bow shock will be transmitted across it and amplified and new waves of various types will be produced in the process. The details concerning the types of waves produced depend on the properties of the incident wave. The power in the variations and complexity of observed forms will be markedly increased by transmission. Interplanetary discontinuities will contribute to magnetosheath variability but they are not frequent enough in the solar wind to explain a significant portion of magnetosheath power. Processes taking place at the magneto-

pause or within the magnetosheath also contribute to observed waves in the magnetosheath.

3.5.2 Bow Shock

The flow of the solar wind past the earth is usually but not always highly supersonic and superalfvenic as far as the protons are concerned. However, both theory and observations imply that the treatment of the bow shock as if it were a hydrodynamic discontinuity is a gross oversimplification. Since the solar wind at earth is collisionless on a scale much larger than the magnetosphere, plasma properties are responsible for producing the bow shock discontinuity, which is a collisionless shock. The types of plasma phenomena involved will depend on the Mach number of the flow, the ratio (β) of the internal energy of the particles to the energy in the magnetic field, and the direction of the magnetic field relative to the shock surface. Figure 3-26 [Greenstadt et al., 1980] shows a conceptualization of collisionless shock phenomena at the earth's bow shock. The magnetic field is visualized as making an angle of about 45° with the solar wind, which is flowing from the direction of
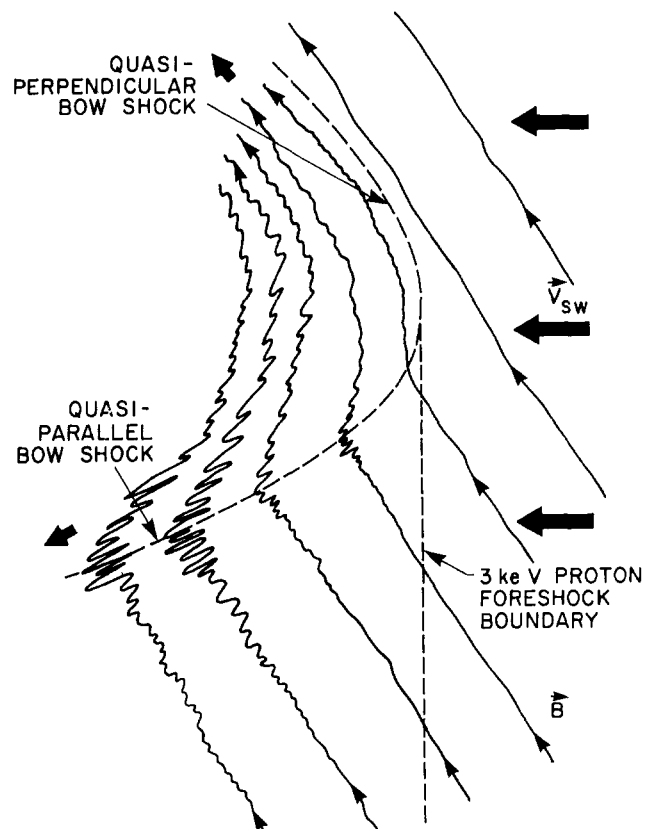

Figure 3-26. A schematic of the earth's bow shock showing the quasi perpendicular and quasiparallel regions. Perpendicular shocks most closely obey the classical magnetohydrodynamic equations but parallel shock region behavior is dominated by plasma effects [Greenstadt et al., 1980; Gary, 1981].

CHAPTER 3

the sun, that is, the sun is beyond the lower right hand quadrant. Four regions of the shock surface are distinguished, the two extremes (strictly perpendicular and strictly parallel shocks) and the two intermediate regions (quasi-perpendicular and quasi-parallel shocks). A shock is called parallel when the upstream magnetic field is perpendicular to the plane of the shock and parallel to the upstream flow velocity. Conversely, perpendicular shocks have normals perpendicular to the direction of the magnetic field in the solar wind. The major part of the bow shock region has been divided into quasi-parallel and quasi-perpendicular regions based on empirical results. Quasi-perpendicular shocks have a monotonic, sawtooth, or wave-step magnetic profile and are sharply defined in space. Quasi-parallel shocks are thicker and do not show a clearly definable boundary between upstream and downstream parameters, either in the field or particle properties.

Figure 3-27 [Greenstadt and Fredericks, 1979] is a schematic of a cut in the plane containing the interplanetary field, showing the waves that appear in the parallel and quasi-parallel region in the vicinity of the classical position of the bow shock. The shocked magnetosheath plasma takes about 5 min to flow around the forward part of the mag-

netosheath so when parameters are averaged over periods of more than 5 min the shock should arrive at the shape given by steady state magnetohydrodynamic theory. The instantaneous shock is not in equilibrium. Figures 3-26 and 3-27 show schematically the waves in the vicinity of the boundary that propagate back into the solar wind and into the magnetosheath. The properties of both the quasi-perpendicular shock and the quasi-parallel shock depend on the range of β and M, where M is the Mach number of the flowing gas. Since the fast wave mode is the MHD wave that steepens into a shock, the Mach number for a perpendicular shock is given by $M = V/(C_A^2 + C_S^2)^{1/2}$ where C_A and C_S are the Alfvén and sound wave velocities. In Table 3-2 [Greenstadt and Fredericks, 1979] the characteristics of shock phenomena are given for various combinations of β and M. A value of $\beta \approx 1$ is the dividing line for the regimes of β parameter space and $M \approx 3$ is the dividing level for the Mach number. An estimate of the incidence of the specific ranges of β and M the solar wind can be found from Table 3-1. In the solar wind β varies from 0.5 to 4.6, and the ranges of sonic and Alfvénic Mach numbers are from 4 or 5 to over 10. However, solar winds with Alfvén numbers less than 1 have been observed on occasion.

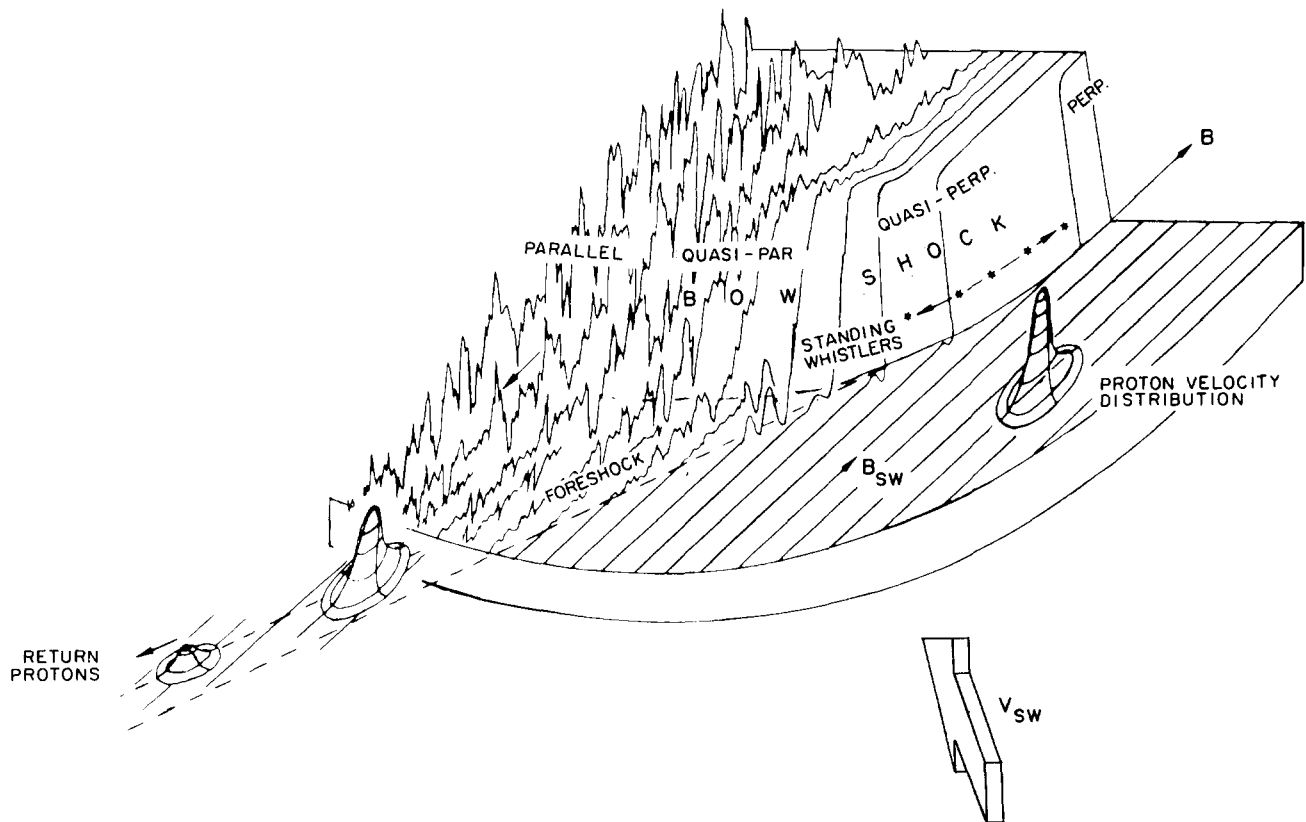Figure 3-27. Conceptualization of collisionless shock phenomenology as manifested in the earth's curved bow shock. Unshocked interplanetary field direction B_{sw} is indicated on the foreground field "platform." Field magnitude is plotted vertically. The superimposed three-dimensional sketches represent solar wind proton thermal properties as number distributions in velocity space [Greenstadt and Fredericks, 1979].

Table 3-2. Macroscopic features of the bow shock by parameter class

Parameter Values	Plasma Conditions	Name of Structure	Quasi-perpendicular Features	Quasi-parallel Features
$\beta \ll$ $M \lesssim 3$	Cold plasma, low Mach number	Laminar	Clean field jump, sometimes with damped periodic waves, no turbulence. Relatively little proton temperature jump $(T_{p2}/T_{p1}) \approx 2$, maxwellian downstream distribution.	Multigradient field transition with embedded, nearly-periodic wavetrains. Upstream waves with strong periodic component, tens of seconds period, unknown plasma distributions.
$\beta < 1$, $M \gtrsim 3$	Cool plasma, high Mach number	Quasi-laminar	Clean field jump, downstream, nearly-periodic waves, little turbulence. Appreciable proton temperature jump, bimodal distribution, nonmaxwellian high energy tail downstream.	Multigradient field transition at least 2 R_E thick, with large amplitude pulses; extensive foreshock. Little change in solar wind streaming velocity; some heating with resulting non-maxwellian proton distributions differing from either solar wind or magnetosheath forms.
$\beta \approx 1$, $M \lesssim 3$	Warm plasma, low Mach number	Quasi-turbulent	Clean field jump, small scale turbulence. Little proton temperature rise, maxwellian downstream distribution.	No known example.
$\beta \approx 1$ $M \gtrsim 3$	Warm plasma, high Mach number	Turbulent	Irregular field fluctuations obscuring definite average field jump. Bimodal or multimodal proton distributions, nonmaxwellian downstream.	Multigradient, irregular field transition with large magnitude excursions, upstream waves. Unknown plasma distributions, but maxwellian deep in magnetosheath.
$\beta \gg 1$ $M > 3$	Hot, high velocity plasma	High-beta	Irregular field fluctuations of extremely high peak magnitude, possibly lowering β locally. Extensive precursor region with appreciable effect on approaching flow; proton distributions unknown.	

(From Greenstadt and Fredricks,[1979])

3.5.3 Upstream Waves and Particles

The solar wind-magnetosphere interaction generates substantial numbers of energetic particles with a high enough speed so that they can propagate back upstream guided by the ambient interplanetary field. The upstream particle region has a strong local time asymmetry with the major effect occurring usually on the dawnside on field lines connected to the quasi-parallel shock. This region of space upstream of the bow shock is sometimes called the foreshock and is characterized by many different types of particle distributions and wave modes. The energy flux of particles into the upstream region is found to be 10^{17}–10^{18} ergs, which is comparable to the peak energy released in a geomagnetic substorm. The presence of energetic heavy ions indicates that strong local acceleration is occurring. Observations of plasma waves, particles, and fields in the region has led to a partial understanding of some of the interrelationships among the phenomena [Tsurutani and Rodriguez, 1981].

The upstream energetic particle population has been divided into several types based on their observed velocity and phase distributions. Reflected ions are characterized by a beamlike distribution of solar wind ions that apparently have been reflected and energized at the bow shock. They have a streaming velocity 2 or 3 times the solar wind velocity and a density of about $0.1/cm^3$. Their kinetic energy distribution typically maximizes at about 5 keV and has spread of 1–30 keV. They are detected on interplanetary field lines that connect to the bow shock and are nearly tangent to the shock surface. The sunward boundary of the region in which these particles are observed is defined by the field-aligned flow back into the solar wind plus $\mathbf{E} \times \mathbf{B}$ convection, where E is the solar wind electric field.

In addition to these beam-like ions there is a population of diffuse ions that has a nearly isotropic velocity distribution with a typical temperature of 4×10^7 K, an upstream flow speed of 0.8–1.2 times the solar wind velocity and a density that varies between 0.02 and $0.8/cm^3$. The

energy density of the diffuse ions is comparable to that of the reflected ions. These particles are found downstream (antisunward) of the reflected ions, almost filling the entire foreshock region. An excellent correlation exists between diffuse ions and low frequency (0.01–1 Hz) MHD and ion-acoustic-like plasma waves. Recent observations indicate that the transition from distributions typical of reflected ions to that of diffuse ions is a smooth one and there are ions with intermediate properties in a region of space between the reflected and diffuse ion region.

Upstream electrons have energies of 0.5 to 100 keV and stream in a field aligned direction. The majority of events involve 1–2 keV particles with a peak flux of $10^4 cm^{-2} s^{-1} sr$ keV^{-1}. They appear on interplanetary field lines newly connected to the bow shock and because of their high velocities can be found upstream of the ion foreshock boundary.

The region upstream from the earth's bow shock is also characterized by complex wave phenomena. There are MHD waves with an amplitude of 5 nT peak to valley and period of 10–60 s, which have a left-hand polarization in the spacecraft frame. The particles involved in the wave show a $\pm$ 15 km/s solar wind velocity variation as well as correlated density fluctuations indicating a magnetosonic component. There is a strong association between these waves and diffuse ions. Wave packets of whistler mode waves having intensities $\leq$ 1 nT and typically composed of 2 or 3 coherent cycles are observed. Long trains of more than 20 cycles have been seen on occasion. The emissions, though left hand polarized in the spacecraft frame have been shown to

be Doppler-shifted right-hand emissions being convected back over the spacecraft. They propagate at small ($\sim$ 25°) angles to the magnetic field. The rest-frame frequencies have been deduced to be 0.1–40 times the proton gyrofrequency. They are related to the MHD waves and are detected during diffuse ion events. Whistler mode waves with frequencies 10–200 Hz are observed upstream of the bow shock. These emissions have a peak amplitude of 0.1 nT and occur at about 1/4 to 1/2 the electron gyrofrequency. It is believed that the most intense waves are associated with low-energy electron spikes coincident with intense diffuse ion fluxes.

Other waves that have been observed include small amplitude electrostatic waves in the 100 Hz–10 kHz range polarized primarily parallel to the ambient magnetic field. They have short wave lengths, 30 < λ < 215 m, and a low relative energy density. Broadband impulsive electrostatic emissions with amplitudes proportional to f^{-2} for frequencies less than 3 kHz are observed to almost always accompany electron plasma oscillations. The electron plasma oscillations themselves have intensities up to 10 mV with wavelengths of 400–780 m and frequencies of 20–30 kHz. They are detected throughout the foreshock region and are driven by 0.2 to 1.5 keV electrons at the boundary of the electron foreshock. Low intensity electromagnetic emissions at twice the electron plasma frequency having a narrow band width are detected upstream of the bow shock to distances of at least 240 R_E. The emission frequency is correlated with solar wind plasma density variations.

REFERENCES

Alksne, A.Y. and D.L. Webster, "Magnetic and Electric Fields in the Magnetosheath," *Planet. Space Sci.*, **18:** 1203, 1970.

Auer, R.D., "Magnetohydrodynamic Aspects of the Earth's Bow Shock 1. Equilibrium Bow Shock Position," *J. Geophys. Res.*, **79:** 5118, 1974.

Bame, S.J., J.R. Asbridge, W.C. Feldman, E.E. Fenimore and J.T. Gosling, "Solar Wind Heavy Ions from Flare-Heated Coronal Plasma," *Sol. Phys.* **62:** 179, 1979.

Barnes, A., "Hydromagnetic Waves and Turbulence in the Solar Wind," in *Solar System Plasma Physics,* edited by E.N. Parker, C.F. Kennel and L.J. Lanzerotti, North Holland, Amsterdam, 1979.

Behannon, K.W. and D.H. Fairfield, "Spatial Variation of the Magnetosheath Magnetic Field," *Planet. Space Sci.,* **17:** 1803, 1969.

Belcher, J.W. and L. Davis Jr., "Large Amplitude Alfvén Waves in the Interplanetary Medium," *J. Geophys. Res.,* **76:** 353, 1971.

Burlaga, L.F., "Micro-Scale Structures in the Interplanetary Medium," *Sol. Phys.,* **4:** 67, 1968.

Burlaga, L.F. and J.H. King, "Intense Interplanetary Magnetic Fields Observed by Geocentric Spacecraft During 1963–1975," *J. Geophys. Res.,* **84:** 6633, 1979.

Burlaga, L.F., E. Sittler, F. Mariani, and R. Schwenn, "Magnetic Loop Behind an Interplanetary Shock: Voyager, Helios and IMP8 Observations," *J. Geophys. Res.,* **86:** 6673, 1981.

Burlaga, L.F. and J.B. Turner, "Microscale Alfvén Waves in the Solar Wind at 1 AU," *J. Geophys. Res.,* **81:** 73, 1976.

Chapman, S., "Notes on the Solar Corona and Terrestrial Ionosphere," *Smithsonian Contrib. Astrophys.,* **2:** 1, 1957.

Coleman, P.J. Jr., "Turbulence, Viscosity and Dissipation in the Solar Wind Plasma," *Astrophys. J.,* **153:** 371, 1968.

Fairfield, D.G., "The Ordered Field of the Magnetosheath," *J. Geophys. Res.,* **72:** 5865, 1967.

Fairfield, D.H., "Magnetic Fields of the Magnetosheath," *Rev. Geophys. Space Phys.,* **14:** 117, 1976.

Feldman, W.C., J.R. Asbridge, S.J. Bame, and M.D. Montgomery, "Interplanetary Solar Wind Streams," *Rev. Geophys. Space Phys.,* **12:** 715, 1974.

Feldman, W.C., J.R. Asbridge, S.J. Bame, M.D. Montgomery and S.P. Gary, "Solar Wind Electrons," *J. Geophys. Res.,* **80:** 4181, 1975.

Feldman, W.C., J.R. Asbridge, S.J. Bame, and J.T. Gosling, "Plasma and Magnetic Fields from the Sun," in *The Solar Output and its Variations,* edited by Oran R. White, Colorado Associated University Press, Boulder, p. 351, 1977.

Feynman, J., "Solar Cycle and Long Term Changes in the Solar Wind," *Rev. Geophys. and Space Phys.,* **21:** 33, 1983.

Feynman, J. and N.U. Crooker, "The Solar Wind at the Turn of the Century," *Nature,* **275:** 626, 1978.

Feynman, J. and S.M. Silverman, "Auroral Changes During the 18th and 19th Centuries and Their Implications for the Solar Wind and the Long Term Variation of Sunspot Activity," *J. Geophys. Res.,* **85:** 2991, 1980.

Gary, S.P., "Microinstabilities Upstream of the Earth's Bow Shock: A Brief Review," *J. Geophys. Res.,* **86:** 4331, 1981.

Gosling, J.T., V.Z. Pizzo, and S.J. Bame, "Anomalously Low Proton Temperatures in the Solar Wind Following Interplanetary Shock Waves—Evidence for Magnetic Bottles?", *J. Geophys. Res.,* **78:** 2001, 1973.

Gosling, J.T., J.R. Asbridge, S.J. Bame, and W.C. Feldman, "Solar Wind Stream Interfaces," *J. Geophys. Res.,* **83:** 1401, 1978.

Gosling, J.T., J.R. Asbridge, S.J. Bame, W.C. Feldman and R.D. Zwicki, "Observations of Large Fluxes of He$^+$ in the Solar Wind Following an Interplanetary Shock," *J. Geophys. Res.,* **85:** 3431, 1980.

Greenstadt, E. W. and R.W. Fredericks, "Shock Systems in Collisionless Space Plasma," in *Solar System Plasma Physics III* edited by C.K. Kennel, L.J. Lanzerotti and E.N. Parker North Holland, Amsterdam, 1979.

Greenstadt, E.W., C.T. Russell and M. Hoppe, "Magnetic Field Orientation and Suprathermal Ion Streams in the Earth's Foreshock," *J. Geophys. Res.,* **85:** 3473, 1980.

Hedgecock, P.C., "Measurements of the Interplanetary Magnetic Field in Relation to the Modulation of Cosmic Rays," *Sol. Phys.,* **42:** 497, 1975.

Hirshberg, J., "The Transport of Flare Plasma from the Sun to the Earth," *Planet. Space Sci.,* **16**(3): 309–319, 1968.

Hirshberg, J., "The Interplanetary Field During the Rising Part of the Solar Cycle," *J. Geophys. Res.* **74:**5841, 1969.

Hirshberg, J., S.J. Bame, and D.E. Robbins, "Solar Flares and Solar Wind Helium Enrichments, July 1965–July 1967," *Sol. Phys.,* **23:** 467, 1972.

Hirshberg, J., Y Nakagawa, and R.E. Wellck, "Propagation of Sudden Disturbances Through a Non-Homogeneous Solar Wind," *J. Geophys. Res.,* **79:** 3726, 1974.

Hundhausen, A.J., *Coronal Expansion and Solar Wind,* Springer-Verlag, New York, 1972.

Neugebauer, M., "The Enhancement of Solar Wind Fluctuations at the Proton Gyroradius," *J. Geophys. Res.,* **80:** 998, 1975.

Neugebauer, M., "Observations of Solar-Wind Helium," *Fundamentals Cosmic Phys.,* **7:** 131, 1981.

Neugebauer, M. and C.W. Snyder, "Mariner 2 Observations of the Solar Wind," *J. Geophys. Res.,* **71:** 4469, 1966.

Neupert, W.M. and V. Pizzo, "Solar Coronal Holes as Sources of Recurrent Geomagnetic Disturbances," *J. Geophys. Res.,* **79:** 3701, 1974.

Ogilvie, K.W., M.A. Coplan, P. Bochsler, and J. Geiss "Abundance Ratios of ^{4}He^{++}/^{3}He^{++} in the Solar Wind," *J. Geophys. Res.,* **85:** 6021, 1980.

Parker, E.N., *Interplanetary Dynamical Process,* Interscience, New York, 1963.

Rickett, B.J., "Disturbances in the Solar Wind from IPS Measurements in August 1972," *Solar Phys.,* **43:** 237, 1975.

Robbins, D.E., A.J. Hundhausen, and S.J. Bame, "Helium in the Solar Wind," *J. Geophys. Res.*, **75**: 1178, 1970.

Russell, C.T., "Geophysical Coordinate Transformations," *Cosmic Electrodynamics*, **2**: 184, 1971.

Schwenn, R., H. Rosenbauer, and K.H. Muhlhäuser, "Singly Ionized Helium in the Driven Gas of an Interplanetary Shock Wave," *Geophys. Res. Lett.*, **7**: 201, 1980.

Scudder, J. D. and S. Olbert, "A Theory of Local and Global Processes Which Affect Solar Wind Electrons 1., The Origin of Typical 1 AU Velocity Distribution Functions, Steady State Theory" *J. Geophys. Res.* **84**: 275, 1979.

Siscoe, G.L., "Evidence in the Auroral Record for Secular Solar Variability," *Rev. Geophys. Space Phys.*, **18**: 647, 1980.

Siscoe, G.L., L. Davis Jr., P.J. Coleman Jr., E.J. Smith, and D.E. Jones, "Power Spectra and Discontinuities of the Interplanetary Magnetic Field: Mariner 4," *J. Geophys. Res.*, **73**, 1968.

Siscoe, G.L., N.U. Crooker, and L. Christopher, "Solar Cycle Variation of the Interplanetary Magnetic Field," *Sol. Phys.* **56**:449, 1978.

Smith, E.J., "Interplanetary Magnetic Fields," *Rev. Geophys. Space Phys.*, **17**: 610, 1979.

Solodyna, C.V., J.W. Sari, and J.W. Belcher, "Plasma and Field Characteristics of Directional Discontinuities in the Interplanetary Medium," *J. Geophys. Res.*, **82**: 10, 1977.

Spreiter, J.R., A.L. Summers, and A.Y. Alksne, "Hydromagnetic Flow Around the Magnetosphere," *Planet. Space Sci.*, **14**: 223, 1966.

Spreiter, J.R. and A.Y. Alksne, "Plasma Flow Around the Magnetosphere," *Rev. Geophys. Space Phys.*, **7**: 11, 1969.

Suess, S.T., "The Solar Wind During the Maunder Minimum," *Planet. Space Sci.*, **27**: 1001, 1979.

Svalgaard, L., "Polar Cap Magnetic Variations and Their Relationship With the Interplanetary Magnetic Sector Structure.," *J. Geophys. Res.*, **78**: 2064, 1973.

Tsurutani, B.T. and E.J. Smith, "Interplanetary Discontinuities: Temporal Variations and the Radial Gradient from 1 to 8.5 AU," *J. Geopys. Res.*, **84**: 2773, 1979.

Tsurutani, B.T. and P. Rodriguez, "Upstream waves and particles: An Overview of ISEE Results," *J. Geophys. Res.*, **86**: 4319, 1981.

Wilcox, J.M. and N.F. Ness, "Quasi-Stationary Corotating Structure in the Interplanetary Medium," *J. Geophys. Res.*, **70**: 5793–5805, 1965.

Wilcox, J.M., L. Svalgaard, and P.C. Hedgecock, "Comparison of Inferred and Observed Interplanetary Magnetic Field, 1970–1972," *J. Geophys. Res.*, **80**: 3685, 1975.